

Article

Behavior of Tantalum in a Fe-Dominated Synthetic Fayalitic Slag System—Phase Analysis and Incorporation

Thomas Schirmer ^{1,*}, Jessica Hiller ², Joao Weiss ³, Daniel Munchen ³, Hugo Lucas ³, Ursula E. A. Fittschen ² and Bernd Friedrich ³

¹ Department of Mineralogy, Geochemistry, Salt Deposits, Institute of Disposal Research, Clausthal University of Technology, Adolph-Roemer-Str. 2A, 38678 Clausthal-Zellerfeld, Germany

² Institute of Inorganic and Analytical Chemistry, Clausthal University of Technology, Arnold Sommerfeld Str.4, 38678 Clausthal-Zellerfeld, Germany; jessica.hiller@tu-clausthal.de (J.H.); ursula.fittschen@tu-clausthal.de (U.E.A.F.)

³ Institute of Process Metallurgy and Metal Recycling, RWTH Aachen University, Intzestr. 3, 52056 Aachen, Germany; jweiss@metallurgie.rwth-aachen.de (J.W.); dmunchen@metallurgie.rwth-aachen.de (D.M.); hlucas@metallurgie.rwth-aachen.de (H.L.); bfriedrich@ime-aachen.de (B.F.)

* Correspondence: thomas.schirmer@tu-clausthal.de; Tel.: +49-5323-722917

Abstract: Pyrometallurgical processes produce slags that may contain valuable elements because of their high oxygen affinity. However, the concentration is extremely low, which causes losses. In fact, these elements, for example, tantalum and rare earth elements, are less than 1% recycled. To return such technologically important elements to the material cycle, pyrometallurgically is used to enrich them in the simplest possible compounds within the slag, which have favorable properties for recovery (morphology, crystal size, magnetic properties), allowing further mechanical separation. The purpose of modification of the slag system is to obtain engineered artificial minerals (EnAM), a process in which targeted minerals with high element concentration are formed. In this article, this approach is investigated using tantalum-rich fayalitic slag, since this slag is commonly found in the industry for the pyrometallurgical treatment of waste electric and electronic equipment. Synthetic fayalitic slags in reducing environment under different cooling rates were produced with Ta addition. The characterization of the produced samples was carried out using powder X-ray diffraction (PXRD) and electron probe microanalysis (EPMA). Additionally, the speciation of Fe and Ta was accessible through X-ray absorption near-edge structure (XANES) spectroscopy. EPMA also provided a semiquantitative assessment of the Ta distribution in these individual compounds. In these slags, tantalum accumulated in perovskite-like oxidic and silicate compounds as well as in magnetic iron oxides. The enrichment factor is highest in tantalite/perovskite-type oxides ($\text{Fe}_x\text{Ta}_y\text{O}_6$, $\text{Ca}_x\text{Fe}_y\text{Ta}_z\text{O}_3$) with up to 60 wt.% Ta and ‘tantalomagnetite’ ($\text{Fe}^{\text{II}}(\text{Fe}^{\text{III}}_{(2.5/3x)}\text{Ta}_x)\text{O}_4$) with a maximum of ~30 wt.% Ta (only fast cooling). This is followed by a perovskite-like silicon containing oxide (XYO_3) with 12–15 wt.% Ta (only slow cooling), and a hedenbergite-like compound (XYZ_2O_6) with a varying content of 0.3–7 wt.%. The Ta concentration in pure Fe, $\text{Fe}_{(1-x)}\text{O}$, hercynitic spinel and hematite is negligible. Despite the very low phase fraction, the most promising EnAM compound is nevertheless perovskite-like tantalum oxide, as the highest enrichment factor was obtained. Tantalum-rich magnetite-like oxides also could be promising.

Keywords: tantalum; mineralogy; engineered artificial minerals (EnAM); iron-rich; synthetic slag; PXRD; EPMA; XANES; thermodynamic modeling



Citation: Schirmer, T.; Hiller, J.; Weiss, J.; Munchen, D.; Lucas, H.; Fittschen, U.E.A.; Friedrich, B. Behavior of Tantalum in a Fe-Dominated Synthetic Fayalitic Slag System—Phase Analysis and Incorporation. *Minerals* **2024**, *14*, 262. <https://doi.org/10.3390/min14030262>

Academic Editors: Kenneth N. Han and M Akbar Rhamdhani

Received: 4 January 2024

Revised: 19 February 2024

Accepted: 26 February 2024

Published: 29 February 2024



Copyright: © 2024 by the authors. Licensee MDPI, Basel, Switzerland. This article is an open access article distributed under the terms and conditions of the Creative Commons Attribution (CC BY) license (<https://creativecommons.org/licenses/by/4.0/>).

1. Introduction

In recent decades, several techniques for recycling waste electrical and electronic equipment (WEEE) have been studied and developed, especially in Europe, where the WEEE directive pushed EU state members to ensure proper treatment of these wastes [1–4].

Primary and secondary copper refiners combine pyro, hydro and electrowinning operations in their processes, dealing with most of the metals in electronics components; thus, this industry is absorbing WEEE as low-grade copper scrap [5–11]. In addition, the recycling of WEEE promotes circular economy, which creates further value to these materials.

Due to the complexity of these materials, which contain organics, base metals (e.g., Fe, Cr, Cu, Ni, Al, Sn, Zn), rare earth elements (REEs, e.g., Nd, Pr), other critical raw metals (CRM, e.g., Ta, Nb), and precious metals (PMs; e.g., Au, Ag, Pd, and Pt), over the years, an adaptation of their unit operations has been developed [2,11–14]. ISASMELT technology was initially applied in Belgium (Umicore, Hoboken, Belgium) and Germany (Aurubis, Hamburg, Germany) to deal with these uncommon scraps [5,15,16]. The result is a metal phase enriched with Cu, Ni, Sn, Cr and PMs and a fayalitic slag phase containing the remaining chemical elements present in WEEE with higher oxygen affinity, such as REEs and Ta, with no possibility of recovery under current recycling strategies due to their low concentration [2,3,12,15,17,18].

The crystalline phases that are formed with the REEs and Ta in the fayalitic slags are still not clear, but it is known that slags from the copper industry contain mainly a mixture of olivine, magnetite (reverse spinel) and amorphous phases [6,19–21]. Because industrial slags are extremely complex, they are far from reaching equilibrium conditions during cooling and complete solidification [22]. If new methods of recovering strategically important minor elements such as Ta are to be sought, it is necessary to know initially how cooling rates and iron speciation affect the final mineralogy and in which crystalline phases these metals might precipitate.

The idea behind knowing which Ta-rich mineral phases can be created is based on the concept of engineered artificial minerals (EnAM). In the case of fayalitic slags, this includes maximizing Fe immobilization in inverse spinel phases (e.g., magnetite), promoting efficient mechanical separation from the bulk mineral phase and concentrating Ta in specific phases that may potentially be recovered through other separation methods (e.g., density separation).

Therefore, this work focuses on studying the behavior of Ta in a synthetic fayalitic slag (SFS) with simplified chemistry by adding a small concentration of Ta and changing cooling rate and evaluating iron speciation. The results of this study are expected to provide essential information for optimizing industrial slags and new strategies for the recovery of CRM such as Ta. The “Background” section contains more explicit information about recovery routes for Ta. In Section 2 (“Background”), typical recovery routes for tantalum bearing waste are introduced. A pure high-temperature (pyrometallurgical) procedure specifically for tantalum-containing waste has not yet been explored in the literature, to the best of our knowledge. Therefore, the work in this article represents a valuable new approach to the recovery of tantalum. One objective of the presented work is a better understanding of the behavior of tantalum in fayalitic slags (especially the dependence of phase formation on the cooling rate) for efficient recovery. The current limitations in this study are still the incomplete concentration of tantalum in one of the suitable phases found. Further studies on cooling rates and cooling curves during solidification are required.

2. Background

2.1. Recovery Routes for Ta

Ta is a scarce element on earth, although its use is spread among medicine (Ta-Nb coating for biocompatibility), industrial applications (coatings against high-temperature corrosion or alloying in superalloys) and electronics. Its use is massively applied in the latter, accounting for 70% of the world’s consumption [23–28]. Ta-based capacitors have better stability and a much higher energy and power volumetric efficiency than other capacitor families, making them indispensable in the miniaturization of electronic components and a key component in 5G technology [29]. New families of Li metal batteries (LMB) also include Ta to enhance the movement and stability of Li ions [30,31].

Several methods have been tested for the separation of Ta from e-waste. Nevertheless, due to the high number of studies on the recycling or upgrading of Ta-containing residues, this section is limited to references that mainly present hydrometallurgical or pyrometallurgical results. A literature search revealed that hydrometallurgy is used to recycle Ta-containing material rather than pyrometallurgy.

Ta is used in the separators of some LMBs. For these, a garnet-like oxide is used (e.g., $\text{Li}_7\text{La}_3\text{Zr}_2\text{O}_{12}$), in which Ta stabilizes the cubic structure [30]. From these compounds, Ta can be recovered hydrometallurgically, either dissolving directly (strong leaching) or in two steps (moderate leaching) with a filtration step to remove the La-Zr-Ta-oxide for a separate leaching step. Both methods are part of a more complex hydrometallurgical process in which concentrated acid must be used in at least one step [30].

Another source of Ta is electronic components that contain capacitors. Since Ta capacitors are mostly installed on printed circuit boards, a first disassembly step is desired to generate a Ta capacitor concentrate. This can be carried out mechanically (e.g., underwater explosion, [32]) in a bath with a eutectic LiCl/KCl melt or with a tin melt [33]. Any remaining embedding resin, housing or solders can be removed with supercritical water (400 °C/25 MPa, [34,35]), with strong bases (NaOH, [36]) or acids (1–3 M HCl, [37]), pyrolytically (880 °C/30 min, [38]) or with ionic liquids like AlCl_3 , dialkylimidazolium halide [39] or bis(trifluoromethylsulfonyl)imides (EBPiP-NTf₂, EOPiP-NTf₂) [40]. In a combined process of disassembly (removal of the resin and wires) and leaching of the milled Ta-containing residue presented by [41], up to 99% of the Ta can be recovered using 5% HF at 220 °C. Ta scrap can also be oxidized with Na_2CO_3 and then dissolved out with a mixture of concentrated H_2SO_4 and HF (50/50) [42]. According to Swain et al., a mixture of HCl and NaF was used to leach Ta scrap, resulting in an efficiency of 99% [42]. FeCl_2 is suitable as a chlorinating agent to obtain TaCl_5 from Ta-containing residue of the reprocessing of Ta capacitors. In air, this then rapidly converts to Ta_2O_5 . The separation efficiency achieved is 93.56% [34].

A third source of Ta is residual products (slag) mainly from the processing of cassiterite (SnO_2) ore [43]. In these slags, Ta is present together with Nb as pentoxide or $(\text{Ta,Nb})_2\text{O}_5$ ([44]). The processing includes various methods for leaching tin slag using acids (HF, HCl, H_2SO_4 , H_3PO_4 , HClO_4), alkalis (NH_3 , NaOH) or NH_4F [43,44]. In those processes, Nantantalate can be produced from Ta_2O_5 contained in the material with NaOH, which can then be converted into fluoro tantalates by means of HF [45]. This soluble product can then be purified with liquid–liquid extraction and used for electrodeposition (e.g., [46]). After leaching of tin slags, further processing of $(\text{Ta,Nb})_2\text{O}_5$ can also be performed by chlorination or carbochlorination at high temperature (up to 1000 °C) with the formation of low-melting placeable TaCl_5 (or TaOCl_3) [47–49]. Tailings from the mining of Ta-bearing deposits (e.g., tantalite/columbite ~ coltan) such as the Penouta mine exist worldwide [50,51]. To reprocess the tailing, tin is first carbothermally separated. The residue is then leached, concentrated and purified via liquid extraction. A mixture of NH_3 and NH_4F is used to separate Nb and Ta.

Low-grade wastes containing 0.5 wt.% of Ta can be subjected to thermal reductions and physical properties separation processes in sequence to originate a so-called synthetic concentrated, in which the Ta_2O_5 concentration reaches 50 wt.% for further use in chemical/metallurgical processes [51].

2.2. Natural Occurrence and Incorporation of Ta into (Slag) Phases

The behavior of an element in forming of slags can be understood through natural analogues. In nature, Ta is pentavalent and mostly oxide-bound. Frequently, compounds of the type AB_2Z_6 , $\text{A}_2\text{B}_2\text{Z}_6(\text{O,OH,F})$, ABZ_3 , and BZ_2 are found. Position A is mostly filled by lower charged and/or larger ions like Na, Ca, Mn, Fe, Y and lanthanides, and U; position B by smaller highly charged HFSE (“high-field-strength elements”) like Ti, Nb, Ta; and position Z by large anions like O, OH and F (e.g., [52]). Ta-bearing silicates or Ta-silicates are not described as naturally occurring minerals.

Some of the literature found deals with the study of Ta-bearing tin slags [53]. In these slags, Ta is bound as simple pentoxide $(\text{Ta,Nb})_2\text{O}_5$ ([44,54]). An unspecified Ta-rich slag contains Ta_2O_5 , TaC, and FeTaO_3 [45].

Apart from the studies on Ta-bearing ores (columbites/tantalites), there are only a few studies on the behavior of Ta in rocks. The correlation between Ti minerals like rutile or titanite and Ta (and Nb) is described in a few works ([54,55]). Elevated concentrations of Ta in ilmenite of up to 245 $\mu\text{g/g}$ were observed by [56].

2.3. Relevant Basic Compounds of Ta

The literature review revealed that the available information on Ta-silicates is scarce. No crystalline phase is documented in the Ta, Si, O system, although atomic layers of stoichiometric Ta-silicates TaSiO_x can be deposited ([57] and references therein). In the system $\text{CaO-SiO}_2\text{-Ta}_2\text{O}_5$, one ternary compound, $\text{Ca}_{10}\text{Ta}_2\text{Si}_6\text{O}_{27}$, is described by [58].

No reference was found on incorporating Ta instead of Si into crystalline silicate structures. Due to the data published by [59], Ta does not occur in tetrahedral coordination, so the substitution of Si with Ta in crystalline silicate structures, e.g., CaSiO_3 , is implausible.

One possibility to incorporate small highly charged ions into silicate crystal structures is pyroxenes with the formula $\text{X}^{[\text{VI}]} \text{Y}^{[\text{VI}]} (\text{Z}^{[\text{IV}]})_2 \text{O}_6$, where, e.g., highly charged and small cations like Ti^{IV} can be incorporated in the Y-position (e.g., augite; see [60]).

A compound, $\text{Ca}(\text{Nb,Ti})\text{O}_{3.33}$, of a comparable nature with the chemically very similar Nb is presented by [61]. Structural analyses revealed that the Ti^{IV} is incorporated in octahedral sites.

Ta can also be incorporated in perovskite-like compounds with the formula $\text{X}_5\text{Y}_4\text{O}_{15}$ [62] and pyrochlore-like compounds with the formula $\text{Ca}_2\text{Ta}_2\text{O}_7$ [63].

As already explained above, Ta is known to be incorporated into natural perovskites ([64], see above, ABZ_3) such as loparite or simpler oxides like ixiolite [52,65,66]. The compounds ilmenite (FeTiO_3) and perovskite (CaTiO_3) also belong to this family. Which of the compounds is formed depends on the size of the A ion. For small cations, the ilmenite lattice is more stable, and, for larger ones, the perovskite lattice is more stable ([66] and references therein). Additionally, natural perovskite (CaTiO_3), tantalite(Fe) FeTa_2O_6 and rynersonite ($\text{Ca}(\text{Ta,Nb})_2\text{O}_6$) all crystallize in the orthorhombic dipyramidal crystal system [65]. In the presence of Ti, up to ~94% of the Ta is incorporated into a perovskite solid solution in synthetic slag [67]. A titanium-Ta oxide with the formula $\text{Ti}^{\text{II}}_{0.33}\text{Ta}^{\text{V}}_{0.67}\text{O}_2$ is presented in the work of [68].

Natural oxides of the structure $\text{X}^{[\text{VI}]} \text{Y}^{[\text{IV}]}_2 \text{O}_4$ mostly do not incorporate small highly charged cations. Exceptions are inverse spinels like ulvospinel $\text{Fe}^{[\text{IV}]2+}(\text{Fe}^{[\text{VI}]2+}, \text{Ti}^{[\text{VI}]4+})\text{O}_4$, where Ti^{IV} is incorporated on one of the octahedral sites [69]. In the titanium oxide rutile, at least the chemically similar Nb can be enriched up to the percentage range (3.77 wt.%, [70]).

The iron oxide Fe_3O_4 (magnetite) can be written as $\text{Fe}^{[\text{VI}]} \text{Fe}^{[\text{IV}]}_2 \text{O}_4$ and therefore belongs to the spinel family. This family of spinel-like oxides also includes titanomagnetite ($\text{Fe}(\text{Fe,Ti})\text{O}_4$), which can contain up to 13 wt.% Ti (e.g., [71]). This corresponds to a stoichiometric factor of 0.6 (recalculated as $\text{Fe}(\text{Ti}_{0.6}, \text{Fe}_{1.2})\text{O}_4$). Referring to the publication of [59], the ionic radii of Fe^{II} and Ta^{V} are comparable in octahedral coordination (0.75 (high spin) and 0.78). Furthermore, the mineral ixiolite Fe^{II} and struverite Fe^{III} occur next to Ta^{V} on the same crystal position [65].

Key takeaways

- The literature survey shows that pyrometallurgical approaches are actually only used in combination with hydrometallurgical processes. A purely pyrometallurgical approach for the recovery of Ta from residual materials does not seem to have been considered so far.
- In nature, Ta is pentavalent and is bound in the form of various oxides. It does not occur in silicates.

- Ta is expected to be incorporated mainly in perovskite-type oxides. Due to the high availability of Si and the usually high viscosity of silicate melts, it is to be expected that part of the Ta is found in more or less amorphous pyroxene-like silicate structures.
- Diadochic replacement of Fe cations with Ta in spinel-like oxides is plausible because of comparable ionic radii and the natural occurrence of oxides like ixiolite [(Ta,Mn,Nb)O₂].

2.4. Basics on Fayalitic Slag

In nonferrous metallurgy, fayalitic-based slag plays a pivotal role in treating various metal scraps such as lead, copper, and WEEE (e.g., Ta) due to its advantageous properties, including low viscosity, a relatively low melting point, and effective iron immobilization within the slag matrix. As the name suggests, fayalitic slags are mainly composed of fayalite (Fe₂SiO₄), which is a prominent iron orthosilicate mineral characterized by its olivine crystal structure. The oxidation state of iron within fayalite can vary between 2+ and 3+, contingent upon the specific crystallographic site and the prevailing oxygen activity in its environment, so the metal content and resulting microstructure of the slag vary significantly depending on the metallurgical treatment process and cooling conditions.

The oxidation of fayalite typically occurs within oxidizing environments, leading to its decomposition into iron oxide, magnetite and/or hematite, along with the formation of silica.

Fayalite is mostly in association with magnetite, constrained by the quartz–fayalite–magnetite (QFM) phase boundary as has been described [20]. The magnetite content in fayalitic slag is influenced by oxygen diffusion and the precipitation of solid mixtures during cooling, contributing to the partially magnetic properties of fayalitic slags at lower temperatures. As the fayalitic slag undergoes the cooling process, fayalite within the slag partially transforms into magnetite and silica [72]. Magnetite, exhibiting an inverse spinel structure, coexists with other compounds in the slag that, under specific conditions, demonstrates magnetic behavior, allowing for efficient recovery using magnetic separators. Researchers and practitioners have reported successful strategies utilizing these magnetic properties to concentrate essential metals such as iron (Fe), titanium (Ti) and vanadium (V) from fayalitic slag, contributing to resource recovery and sustainability in the metallurgical industry [73,74].

3. Materials and Methods

3.1. Materials and Sample Preparation

To produce the SFS, the following raw materials were used in powdered form: reagent-grade Fe₂O₃ (99.99 wt.%) and CaO (≥95 wt.%) from the company Thermo Fischer GmbH (Kandel, Germany), Fe electrolytic (≥99 wt.%) from Allied Metals GmbH (Düsseldorf, Germany), commercial-grade SiO₂ (≥99.99 wt.%) from Heraeus Quarzglas GmbH & Co. KG (Hanau, Germany), and Al₂O₃ (≥99.6 wt.%) from Nabaltec AG (Schwandorf, Germany). To achieve a weight fraction of 55% of FeO, the synthetic slag was prepared with 40.75 g of Fe₂O₃ and 14.25 g of electrolytic Fe. This favors the formation of fayalite, stabilizing iron in the slag phase [7,8]. The other components and their weight were 25 g SiO₂, 15 g CaO, and 5 g Al₂O₃. The addition of alumina and lime aims to reduce the melting temperature. Finally, the source of Ta was commercial capacitors (Bürklin, type C, Bürklin, Oberhaching, Germany) without molded epoxy cases and connectors. The Ta concentration in WEEE slags generated in the past is less than 500 ppm; nevertheless, the number of capacitors added to the melt guarantees a Ta concentration of approximately 8000 ppm, which was chosen due to the analytical detection limit of the characterization techniques utilized in this study. The theoretical composition is listed in Table 1.

Table 1. Theoretical composition of the used artificial slag.

wt.%	Fe ₂ O ₃	Fe	SiO ₂	CaO	Al ₂ O ₃	Ta
	40.43	14.14	24.80	14.88	4.96	0.80

All these compounds were then mixed, added to a sintered alumina crucible (C799) with 5 cm of internal diameter, and heated (300 °C/h) in an electric resistance heating furnace (Gero HTRV 100-250/18) under an air atmosphere until reaching 1350 °C. Once the target process temperature was reached, the melt was held for 2 h. Subsequently, three cooling rates under an argon atmosphere with a constant flow of 5 L/min were used to evaluate the influence of Fe speciation and mineralogy: 300 °C/h (sample S300), 200 °C/h (sample S200), and 50 °C/h (sample S50) until reaching room temperature. In addition, for XANES analysis, an extra pair of samples containing a high Ta concentration was produced with cooling rates of 300 °C/h (sample HS300) and 50 °C/h (sample HS50). These samples were prepared using powdered Ta₂O₅ (99.99 wt.%, Sigma Aldrich), and the concentrations were adjusted to 10,000 ppm to suit the analytical requirements.

After synthesis, the samples were mechanically liberated from the crucibles. The slag was separated from the iron nugget at the bottom for further processing. Some larger slag grains were retained for preparing thin sections for EPMA analysis. The rest of the slag material was milled to a fine powder.

3.2. Thermochemical Modeling and Simulation

The calculations and simulations use the same starting component and concentration described above. The smelting process was simulated using FactSage 8.2TM “Equilib” module, combining FactPS (database of pure substances) and Ftoxid (database containing oxide solutions and other components, version 8.2) [75]. Models were carried out using an oxygen partial pressure of 10⁻¹¹ bars, varying the concentration of metallic Fe in the model between 0 and 15 g to simulate iron dissolution and temperatures increasing up to 1300 °C. It is important to highlight that Ta-containing phases are limited in commercial thermodynamic databases; thus, one of the main outputs of this work is to include the discovered Ta phases in future model simulations. Nevertheless, considering that Ta is a minor element in the slag (concentration in ppm), it is expected that the modelling of the slag system is still valid for explaining the bulk mineralogy.

3.3. Methods of Analysis

3.3.1. Speciation Analysis with XANES

X-ray absorption near-edge structure (XANES) spectroscopy was applied to determine the Fe and Ta species in the slags. For this purpose, the following standard materials were used: Fe foil fixed in an Al frame from Exafs Materials (Danville, CA, USA), olivine (mineralogical collection, TU Clausthal), Fe₂O₃ (99.9%) from ThermoFisher GmbH (Kandel, Germany), Fe₃O₄ (95%) from Sigma-Aldrich (St. Louis, MO, USA), Ta foil fixed in an Al frame from Exafs Materials (Danville, CA, USA), TaC (99.5%) from ThermoFisher GmbH (Kandel, Germany), TaN (99.5%) from ThermoFisher GmbH (Kandel, Germany), Ta₂O₅ (99.99 wt.%, Sigma Aldrich), and tantalite (mineralogical collection, TU Clausthal). The olivine served as a proxy compound for pure fayalite Fe₂[SiO₄]. Besides the element foils, the standards as well as the slags were present as finely ground powders. For the XANES measurements, these powders were prepared as pellets with a diameter of 16 mm. Therefore, a certain amount of the respective powder was meticulously mixed with 80 mg of Uvasol[®] polyethylene powder as a binder (Merck KgaA, Darmstadt, Germany) in an agate mortar. Subsequently, the mixture was transferred into the pressing dye. With an MP250 laboratory press (Maassen GmbH, Reutlingen, Germany), a pressure of 10 t was applied for two minutes. Additionally, a blind pellet containing only the binder was analogously prepared. The used weight portions of the standards and the slags depended on the actual element content, ranging from 10 to 80 mg.

The XANES measurements were performed with a lab-based easyXES100-extended spectrometer (easyXAFS, LLC, Renton, WA, USA) in transmission mode. The device was equipped with an air-cooled X-ray tube comprising a Pd anode, Si110 as a spherical bend crystal analyzer, a silicon drift detector and a helium box [76]. The Fe K-edge was probed in the energy range of 6930–7400 eV, whereas the Ta L_{III}-edge was examined in the energy range of 9723–10,181 eV. The edges were scanned with energy steps of 0.25 eV and a measurement time of 4 s and 2 s per step, respectively. Additionally, the Ta L_I-edge was investigated (see the Appendix A for further information). Five repetitive measurements of the slags were performed; the spectra were merged in the subsequent data processing. The recorded I₀ and I_t spectra were processed in the software HERMES, version 1.0.0 [77]. Energy calibration was performed by calculating the first derivative from the spectra of the measured element foils and setting the first maximum to the respective edge energy reported by Bearden and Burr [78]. The K-edge of Fe⁰ was set to 7112 eV, and the L_{III}-edge of Ta⁰ was fixed to 9881 eV. Normalization and linear combination fitting (LCF) were conducted with ATHENA software, version 0.9.26 [79].

3.3.2. Chemical Bulk Analysis

A fraction of the sample was digested with a mixture of nitric acid, hydrochloric acid and hydrofluoric acid in a TurboWAVE digestion autoclave from MLS. Another fraction was melted with lithium tetraborate in a platinum crucible at 1050 °C for 20 min, followed by leaching with dilute hydrochloric acid. The bulk chemistry of the two digestion solutions was determined using ICP-OES (ICP-OES 5100, Agilent, Agilent Technologies Germany GmbH & Co. KG, Waldbronn, Germany).

3.3.3. Mineralogical Investigation

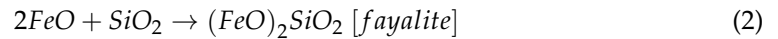
The bulk mineralogical composition was determined with powder diffraction (PXRD) using backloading specimens. A Malvern Panalytical X-Pert Pro diffractometer was used, equipped with a co-X-ray tube and a Malvern Panalytical PIXcel1d (Malvern Panalytical GmbH, Kassel, Germany). The scan range was 5–100 °2θ with a step width of 0.026 °2θ and a measurement time of 12 min (Malvern Panalytical GmbH, Kassel, Germany). Identification was performed using the pdf-2 ICDD XRD database [80], the open crystal database [81] and the Materials Project [82]. The diffractometer was regularly checked to ensure the accuracy of the angular positions using a special pure silicon crystal specimen.

Spatially resolved point and line analysis of crystals and grains was performed using electron probe microanalysis (EPMA, (CAMECA SAS, Gennevilliers Cedex, France). Chemical characterization of individual points or line scans was performed using wavelength-dispersive or energy-dispersive X-ray fluorescence (WDX or EDX). Electron optical images were generated using backscattered electron images with atomic number contrast (BSE(Z)). Measurements were performed with a Cameca SX FIVE FE Field Emission electron probe equipped with a Schottky electron emitter, SE and BSE detectors, and five wavelength dispersive (WDX) spectrometers (CAMECA SAS, Gennevilliers Cedex, France), among others equipped with LTAP (large, thallium phthalate), LPET (large, pentaerithritol) and LLIF (large, lithium fluoride) and LIF (lithium fluoride) crystals. Using an appropriate set of these analytical crystals, the points were analyzed with 15 kV/30 nA for the elements/(crystal, lines): Mg/(LTAP, Kα), Al/(LTAP, Kα), Si/(LTAP, Kα), Ca/(LPET, Kα), Fe/(LIF, Kα) and Ta/(LLIF, Lα). Reference materials from P&H Developments Ltd. (Glossop, Derbyshire, UK) and Astimex Standards Ltd. (Toronto, ON, Canada) were used for calibration. Line overlap correction was applied for SiKα (1st order) on TaLα. Before each calibration, the angular accuracy of the spectrometers was checked on suitable international reference materials (verify procedure). Selected peaks were checked again on the samples and adjusted if necessary to compensate for any chemical shifts that may occur. The beam size setting was 0 (zero), which allowed a diameter well below 1 μm (Schottky-type beam diameter, see, e.g., Jercinovic et al. [83]). Matrix correction was performed using the X-PHI model [84].

4. Results

4.1. Thermochemical Modelling and Simulation

In this research, the use of hematite (100% Fe^{III}) and Fe⁰ allowed the iron speciation to be changed, taking into account that once the liquid phase is reached, there is a high oxygen partial pressure, which is entirely related to the concentration of Fe ions [85,86]. According to the following equations, for every mole of Fe transferred into the slag, at least three moles of FeO will be created, promoting the formation of fayalite.



Thermodynamic simulation performed in FactSageTM where the initial composition described in Section 3.1 was used as input data, and the diagrams in Figure 1a,b were built. Without using oxygen lances, as in industrial processes, the integration of metallic Fe into the slag depends exclusively on the reaction of Equation (1) and the oxygen diffusion from the slag surface in contact with air, once the metallic phase at the bottom of the crucible is difficult to be reached [7,85,87,88]. Figure 1a shows that as iron is gradually integrated into the mineral phase, there is a positive evolution of the liquid phase (green area), which is followed by total reabsorption of hematite, which will be transformed into magnetite following Equations (1) and (3), and, finally, when more than 75% of Fe is integrated, the slag becomes purely fayalitic. The increase in FeO in the mineral phase raises the basicity, reducing the melting point and viscosity.

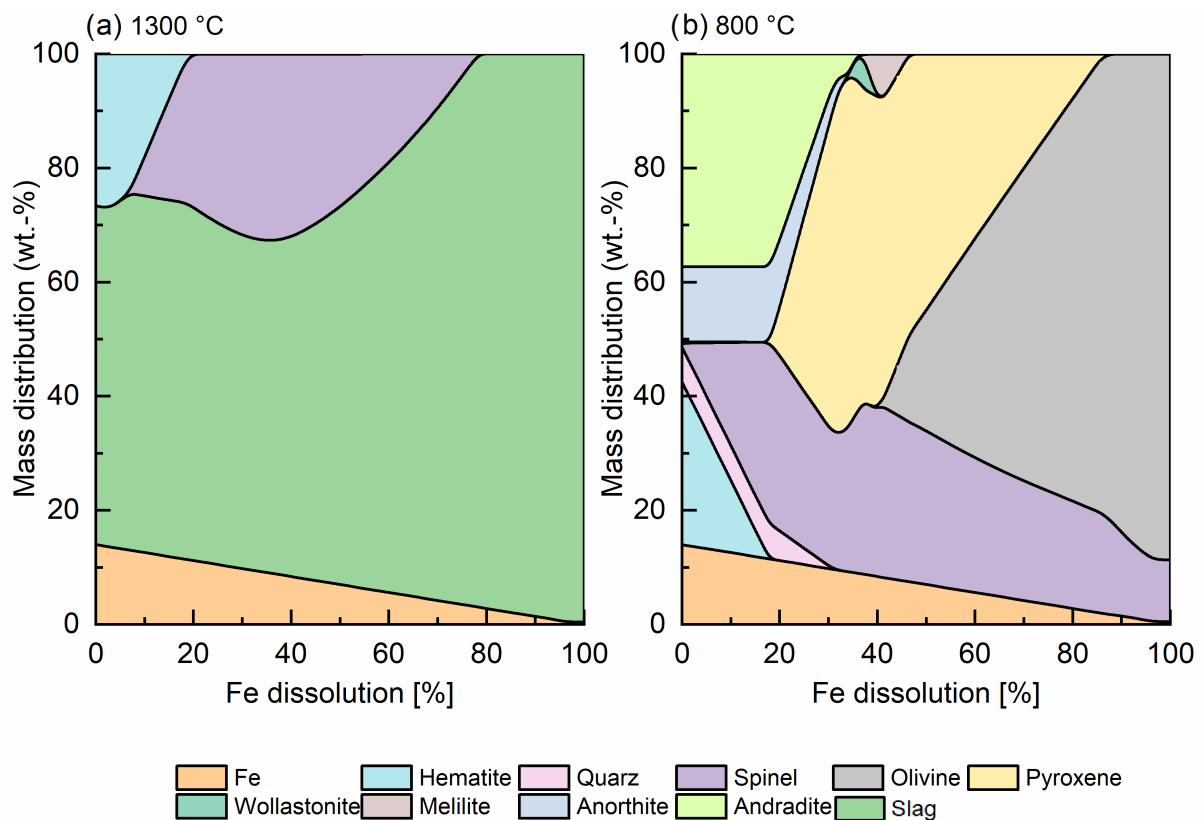


Figure 1. Thermodynamic simulations in FactSage 8.2TM at equilibrium in two different temperatures (a) 1300 °C and (b) 800 °C, where the Fe dissolution (%) is plotted against the mass distribution (wt.%) of a synthetic fayalite slag according to the input composition (Section 3.1).

Fe speciation plays a major role in the properties of fayalitic slags. Thermodynamic models do not describe the influence of kinetics. If all the metallic Fe is integrated, the system will always evolve to give results close to the 100% Fe dissolution model. However, from the kinetic point of view, the longer the test time, the closest to equilibrium.

Figure 1b shows the model result at 800 °C, and it can be observed that the content of olivine phases, e.g., fayalite, increases with higher iron dissolution to the detriment of pyroxenes (e.g., hedenbergite and augite) and spinel (magnetite as the main phase). Theoretically, at high temperatures, in the presence of silica, Fe^{II} should prevail, but as the mineral cools down, the system should evolve by absorbing oxygen for the total re-transformation of Fe^{II} into Fe^{III} again. From the kinetics point of view, at lower temperatures (<500 °C), such conditions will never be achieved. Decades of experience working with fayalitic slags has shown that given the complexity of the system and the low oxygen diffusion, below 800 °C, the system could still evolve from a mineral point of view. However, the available energy is too low to reach thermodynamic equilibrium, and the slag mineralogy freezes close to it.

4.2. Speciation Analysis of Ta and Fe

Two Ta-rich slags (HS50 and HS300) with target Ta concentrations of metallic 10 wt.% had to be specifically synthesized for the speciation of Ta in order to be well above the detection limits (see Section 3.1). The recorded and processed Ta L_{III}-edge XANES spectra of the references and the synthetic slags were compared to determine the species contained in the samples. The oxidation states of the standard materials ranged from Ta⁰ in Ta foil to Ta^V in Ta₂O₅ and tantalite. TaN and TaC belong to interstitial compounds in which tantalum is formally present as Ta^{III} and Ta^{IV}, respectively. Since these types of compounds often have non-stoichiometric compositions, variations from the formal species are possible [89,90].

Figure 2 shows the normalized spectra of the standard materials and the two slags HS50 and HS300. A very prominent feature in the spectra is the white line. This signal mostly bases on allowed 2p to 5d transitions and usually has a higher intensity for oxidized species due to an increased number of vacant 5d states [91]. Unfortunately, the influence on the signal height is not as strong and consistent among the standard materials as expected from other d-elements like rhenium (Re) [92–94]. Furthermore, the energy shift of the Ta L_{III}-edge is barely influenced by the oxidations state of the absorbing atom and would lead to relatively high errors of species determination [94]. However, conclusions of the species can be derived from the position of the white line and its fine structure as well as from the first oscillations in the post-edge region. The qualitative comparison of the spectra shows high similarity between the slags with Ta₂O₅ and tantalite. This is attested by the position of the white line at around 9886 eV (blue arrow) as well as by the evolving broad signal at approx. 9935 eV (yellow arrow), which seem to be characteristic for Ta^V species. TaC and TaN also show a broad signal, but this is located at approx. 9929 eV; the spectrum of the Ta foil does not have an elevated signal in either of the mentioned regions. Furthermore, a detailed look at the form of the white line reveals a flattened and slightly split maximum in the case of tantalite and the two slag samples (Figure 3).

The splitting features depicted with A1 and A2 are already known in the literature [94–97]. According to the white line, splitting can be directly explained by the influence of the ligand field on the 5d orbitals, which causes the separation of the 5d levels into t_{2g} and e_g orbitals [95,98].

The speciation of Fe was performed on the low-Ta slags S50, S200 and S300, which were synthesized with three different cooling rates (3.1). In Figure 4, the normalized Fe K-edge XANES spectra of the standard materials and the slags are depicted. The corresponding formal oxidation states include Fe⁰ in the foil, Fe^{II} in olivine, a 1:2 mixture of Fe^{II} and Fe^{III} in Fe₃O₄ and Fe^{III} in Fe₂O₃. Olivine served as proxy material for fayalite, since pure fayalite was not available. The similarity of their X-ray absorption was confirmed by comparing the recorded XANES spectrum of olivine with a XANES spectra of fayalite deposited in the database Hephæstus [80,99,100].

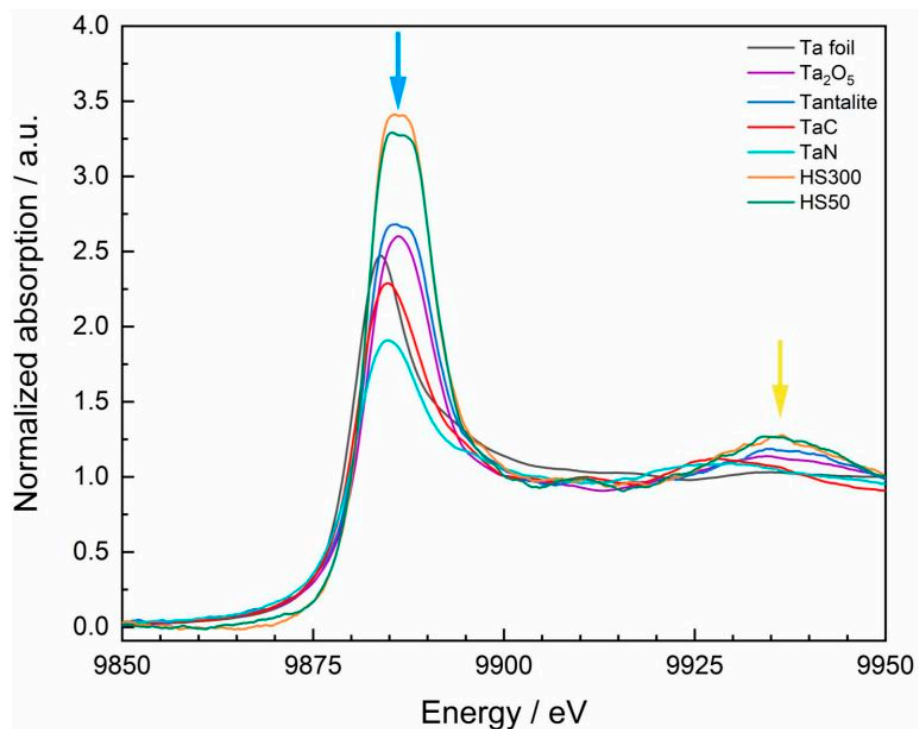


Figure 2. Ta L_{III}-edge XANES spectra of the standard materials (Ta foil, Ta₂O₅, tantalite, TaC and TaN) and the high-Ta slag samples (HS50 and HS300). The L_{III}-edge of Ta⁰ is located at 9881 eV. Blue arrow: White line at around 9886 eV, yellow arrow: Evolving broad signal at approx. 9935 eV. Further description in the text.

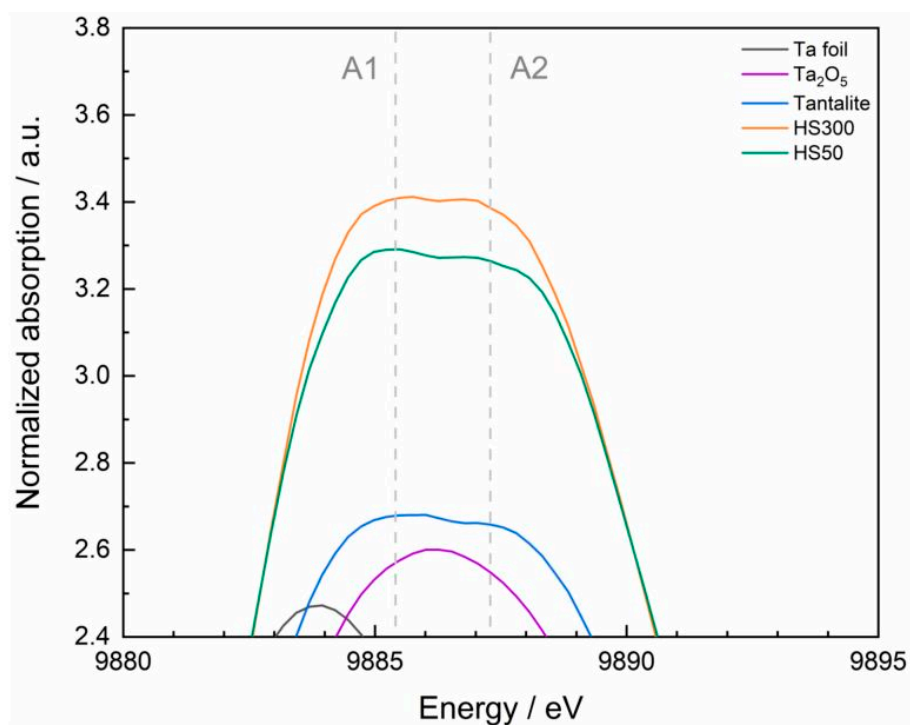


Figure 3. Detailed view of the white lines of the Ta L_{III}-edge XANES spectra from Ta₂O₅, tantalite, sample HS50 and sample HS300. Splitting features are indicated with the dashed vertical lines as well as with the terms A1 and A2.

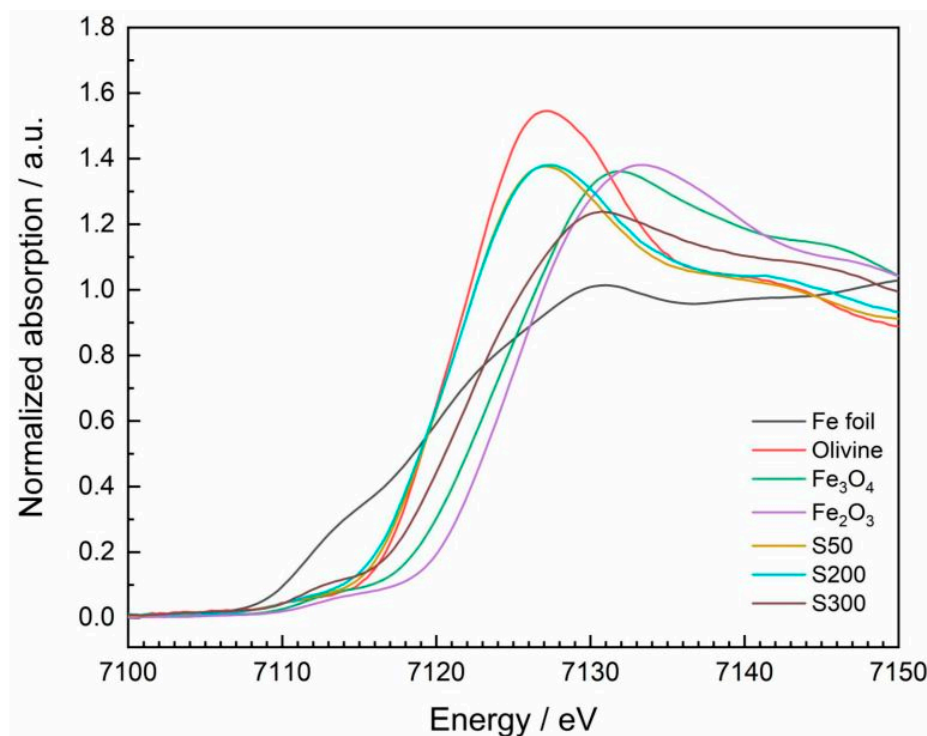


Figure 4. Fe K-edge XANES spectra of the standard materials (Fe foil, olivine, Fe_3O_4 , Fe_2O_3) and the low-Ta slag samples (S50, S200 and S300). The K-edge of Fe^0 is located at 7112 eV.

All spectra show a weak pre-edge peak at around 7113 eV due to quadrupole 1s to 3d transitions as well as a pronounced white line based on dipole allowing 1s to 4p transitions [91]. In contrast to the investigation of the Ta L_{III} -edge, the pronounced edge shift of the Fe K-edge allows for reasonably identifying the corresponding formal oxidation state. Consistent with the literature, the K-edge shifts towards higher energies for compounds bearing iron in a higher oxidation state [100]. Referring to the foil that contains iron as Fe^0 and which edge is positioned at 7112 eV, a maximum shift of approx. +13 eV is obtained for the species Fe^{III} in Fe_2O_3 . In linear combination fitting (LCF), a region of -20 eV to $+80$ eV with respect to the edge position of the slags was considered. The spectra of the slags as well as that of olivine and tantalite were previously smoothed using a box car average algorithm implemented in ATHENA. To overcome uncertainties due to deviations of the normalizations, the sum of the fitted fractions was not forced to equal 1. Initially, all standard materials listed above were considered in the LCF. Only the combinations that led to fit results having the lowest r-factor and the lowest single error relative to the respective fraction were considered for further evaluation. Finally, the best fits only included fractions of elemental iron (here as Fe foil), olivine and magnetite. Figure A1 (Appendix A) shows the best fits and the corresponding residuals. The underlying percentages of the fractions were allocated to the iron species contained in the standard materials. The Fe^0 proportion was found to be nearly constant with an average value of $21 \pm 1\%$ for all three slag samples. Since dampening effects might influence the spectra and suggest that Fe^0 is the best option for a third component, also LCF with only olivine and magnetite were evaluated. To interpret the influence of the cooling rate on the iron speciation in the slags, the portion of Fe^{II} in total iron-containing slag phases ($\text{Fe}^{\text{II}} + \text{Fe}^{\text{III}}$) was calculated. Table 2 lists the results of the iron speciation.

Table 2. Results from iron speciation in the slags based on LCF of the XANES spectra.

Sample	Cooling Rate/°C/h	Fraction of Fe ^{II} in Total Fe ^{II} + Fe ^{III} System/%
S50	50	100–91.3
S200	200	96.6–89.6
S300	300	49.9–52.0

Depending on the cooling rate with which the slags were formed, the portion Fe^{II} in total iron-containing slag phases (Fe^{II} + Fe^{III}) changes. While for S50 and S200 the highest portions of Fe^{II} were found, S300 contains nearly as much Fe^{III} as Fe^{II}. Hence, it can be stated that the amount of Fe^{II} decreases with increasing velocity of the cooling process. This trend is obviously non-linear; based on the investigations, a significant formation of Fe^{III} can be expected within the cooling rate of 200–300 °C/h. Between 50 °C/h and 200 °C/h, the Fe^{II} species dominates.

4.3. Bulk Chemistry

The bulk chemical analysis results for the three synthetic slags (Table 3) show deviations from the theoretical initial values. This is due to the fact that a varying amount of undissolved metallic iron was still present in each sample produced, regardless of the cooling rate used, resulting in a variation in the residual sample. XANES results in Table 2 confirm these results, showing that around 80% of metallic iron was dissolved in the slag. Since the source of Ta came from capacitors, there are also traces of other elements.

Table 3. Results of the bulk chemical composition, in percentages, of three synthetic slag experiments.

wt.%	300 °C/h	150 °C/h	50 °C/h	Method
Al ₂ O ₃	7.2	5.9	8.4	XRF
CaO	14.9	16.8	11.9	XRF
SiO ₂	25.7	25.3	23.0	XRF
FeO	50.9	50.9	54.6	XRF
MnO	0.2	0.2	0.3	XRF
P ₂ O ₅	0.1	0.1	0.1	XRF
Cr ₂ O ₃	0.1	0.0	0.1	XRF
NiO	0.0	0.0	0.2	XRF
Na ₂ O	0.0	0.1	0.0	XRF
Ta	0.50	0.42	0.66	ICP-OES

4.4. Mineralogical Characterization

4.4.1. Morphology

The morphology was investigated using BSE(Z) micrographs. In the following sections, each cooling rate will be investigated.

Cooling Rate of 300 °C/h

At the relatively high cooling rate of 300 °C/h (S300), large spinel crystals surrounded by a massive Ca-Al-silicate matrix with initial crystallization can be seen in the backscattered electron image (Figure 5, upper left, Z-contrast). Even the spinel crystals show hypidiomorphic crystal habitus and signs of skeletal growth. In some parts of the sample, the spinel crystals are partially surrounded by brighter rims. In other parts of the sample, elongated crystals of a heavy element compound can be observed (Figure 5). The EDX spectra show that the spinel has a magnetitic composition with a few weight percent of aluminum. The brighter edges show an increased Ta concentration (Figure 5, lower left "A"). The partly lath-shaped bright crystallites show a very high Ta content (Figure 5, lower left "B").

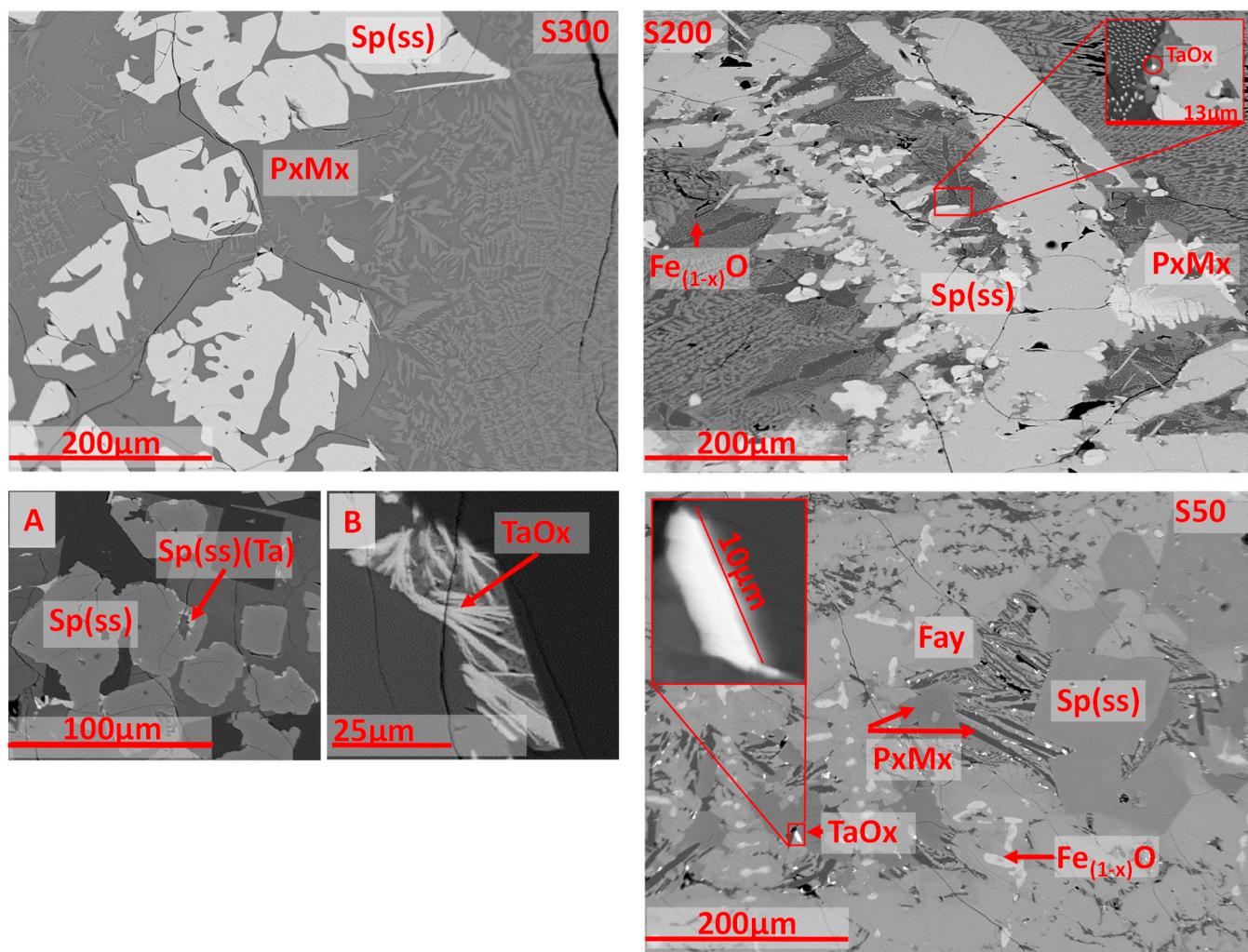


Figure 5. BSE(Z) micrographs of selected areas of the three samples. S300: Overview of a typical part of the sample, below two detailed images with Ta-containing spinel (left) and Ta oxide (right). S200: Overview of a typical part of the sample. S50: Overview of a typical part of the sample. PxMx: pyroxenitic matrix, Sp(ss): spinel solid solution, Fay: fayalite. For further descriptions, see text.

Cooling Rate of 200 °C/h

The sample cooled moderately fast at 200 °C/h (S200) shows giant growth of spinel with beginnings of skeletal growth. Furthermore, oval xenomorphic crystals of iron oxide are visible. This is surrounded by a clearly crystallized Ca-Al-silicate matrix with dendritic-to-skeletal growth (Figure 5, upper right). Sporadically, μm-sized grains of a light-colored heavy element compound are found (Figure 5, upper right, small detail image). The EDX shows that this spinel is of magnetitic composition with a few weight percent of aluminum. The oval crystallites show a very high iron content, so that it should be a kind of wustite (Fe_{1-x}O). The small bright grains show a very high Ta content (>50 wt.%).

Cooling Rate of 50 °C/h

At a comparatively slow cooling rate of 50 °C/h (S50), idiomorphic spinel crystals appear in a matrix of fayalite and Ca-Al silicate (Figure 5, lower right). Furthermore, iron oxide and a bright heavy element compound are present in this matrix. According to EDX, the spinel has a magnetitic–hercynitic composition (>20 wt.% Al), and due to the high iron content, the iron oxide is most likely Fe_{1-x}O. The light-colored heavy element compound shows a very high Ta content (>50 wt.%). The grain size is in the 10 μm range.

4.4.2. Detailed Phase Analysis

For a first overview of the phase analysis, powder diffraction was first conducted on all samples. This result provided a first impression of the expected phases for the EPMA, which was used to determine the exact chemical composition of selected points. In the following, the result of the PXRd for the synthetic slags with the three different cooling rates is presented first and then extended with the result of the spatially resolved EPMA.

No Ta-rich compound was found with the PXRd. This is also not to be expected due to the overall low concentration of Ta.

From the relatively complex diffractograms, three interesting regions could be extracted: 23–29 °2θ with different lattice planes of fayalite ($\text{Fe}^{\text{II}}_2\text{SiO}_4$) and kirschsteinite ($\text{CaFe}^{\text{II}}\text{SiO}_4$), 34–37 °2θ with lattice planes of pyroxenitic matrix silicates (hedenbergite/Augite/ $\text{CaFe}^{\text{II}}\text{Si}_2\text{O}_6$ — $(\text{Ca},\text{Na})(\text{Mg},\text{Fe}^{\text{II}},\text{Al},\text{Ti})(\text{Si},\text{Al})_2\text{O}_6$), and 67–77 °2θ with relatively free peaks of spinels and Fe_{1-x}O .

In the first region (Figure 6), no peaks are present at 300 °C/h cooling. At 200 °C/h, there is no peak near the database pattern of fayalite, but only in the middle between the patterns of kirschsteinite and fayalite. At 50 °C/h, two peaks show up, one very close to the database pattern for fayalite and the other lying between the patterns for fayalite and kirschsteinite.

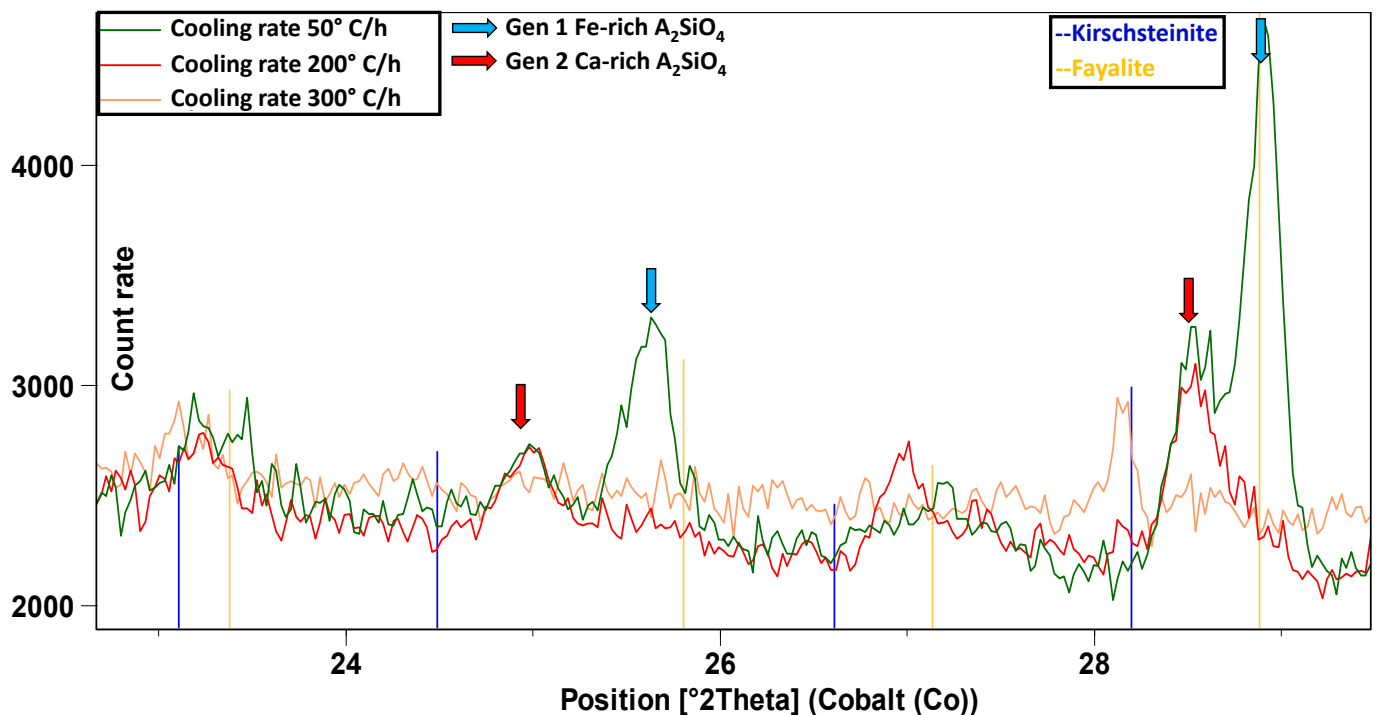


Figure 6. Section of the PXRd in the angular range 23–29 °2θ. Explanations in the text.

In the second region (Figure 7), distinct peaks at 300 °C/h show up only around the patterns of augite/hedenbergite and magnetite. Due to line overlap, the presence of small amounts of esseneite cannot be excluded. At 200 °C/h, there are clear peaks also in the area of the patterns of augite/hedenbergite, magnetite and with lower probability between magnetite and hercynite. Moreover, here, the presence of small amounts of esseneite cannot be excluded. At 50 °C/h, there are clear peaks also in the area of the patterns of augite/hedenbergite and between magnetite and hercynite. In addition, a peak is seen near the 100% pattern of fayalite. Again, here, the presence of small amounts of esseneite cannot be excluded.

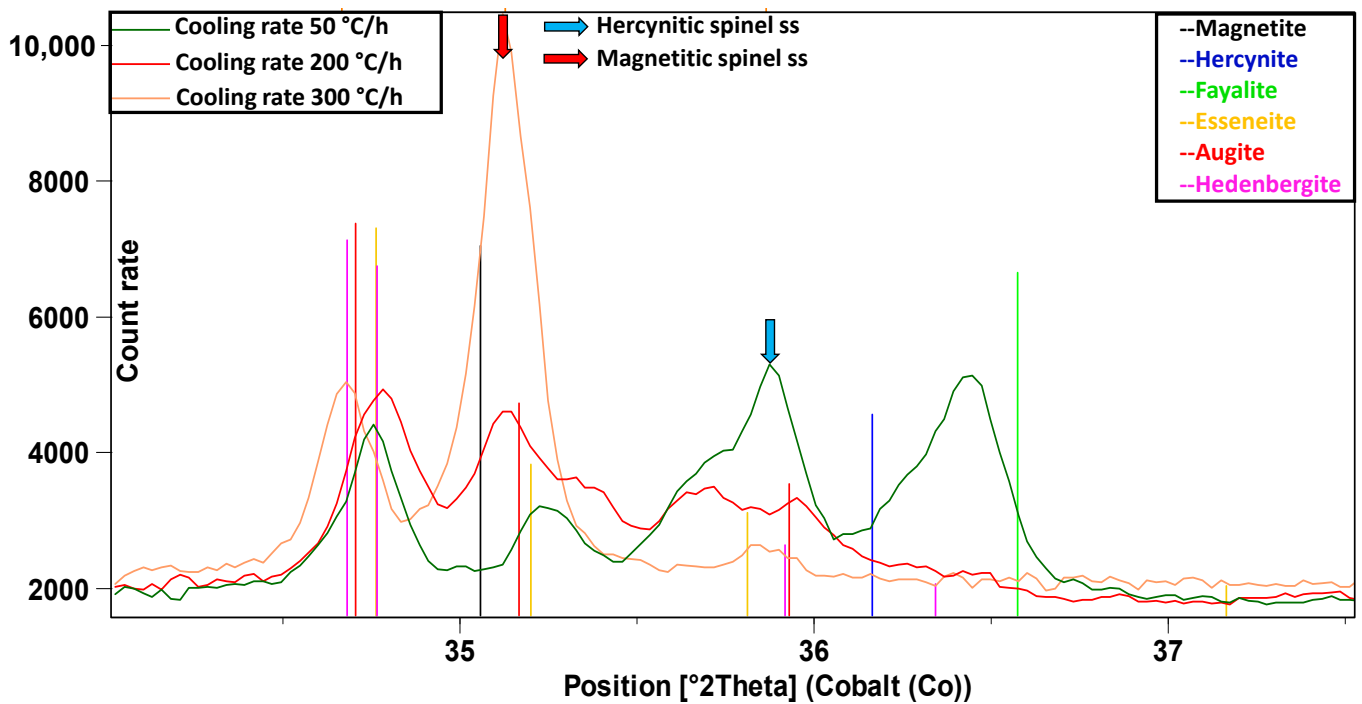


Figure 7. Section of the PXRD in the angular range 34–37 °2θ. Explanations in the text.

In the third angular range (Figure 8), only magnetite can be clearly detected at 300 °C/h, with the peaks shifted towards the pattern of hercynite at smaller angles. At 200 °C/h, wustite (Fe_{1-x}O) and magnetite with peaks also shifted towards hercynite can be observed. At 50 °C/h, only peaks between the patterns of hercynite and magnetite are found.

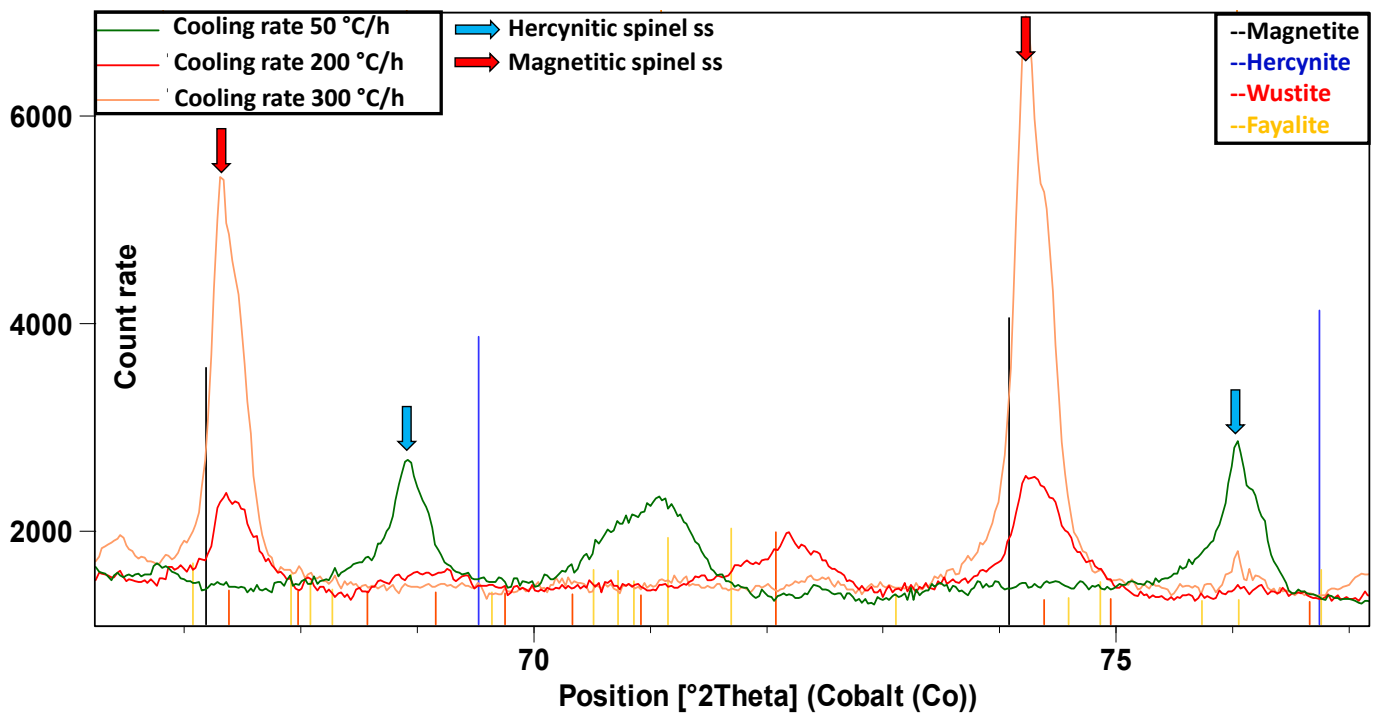


Figure 8. Section of the PXRD in the angular range 67–77 °2θ. Explanations in the text.

The EPMA results basically confirm the PXRD observations but also show additional compounds. An overview of Ta-rich compounds is given in Table 4. The observed compounds in total are as follows:

- Oxides: Ta-oxides with Ta concentration with max. close to 70 wt.% Ta.
- Al containing magnetite spinel (solid solution) with max. 30 wt.% Ta.
- Fe-rich hercynitic spinel with low Ta concentration.
- Iron oxides $\text{Fe}_{1-x}\text{O} \rightarrow$ hematite with low Ta concentration.
- Silico-oxide perovskite-like silicon containing oxide with max. 14.5 wt.% Ta.
- Silicates: Ca-Al-silicate (more hedenbergitic, perhaps partly amorphous) with Ta up to ~6–7 wt.% Ta.
- Fayalite—kirschsteinite (fayalite(Ca) solution) with very low Ta concentration.
- Esseneite with very low Ta concentration.
- Elements: Pure Fe with virtually no Ta.

Table 4. Examples of Ta-rich compounds in the three synthetic slags. Base Comp.: theoretical stoichiometric formula. A in ABO_3 : Ca, Fe^{II} , Ta, B in ABO_3 Al, Si, Ta. Min.–Max.: minimum–maximum, Ave.: average, Rel. StDev. (%): relative standard deviation, n.a.: Not applicable. Rel. StDev. (%) for traces is not included. Due to the high variability, the Ta-containing pyroxene (hedenbergitic) matrix is given as a min.–max. range.

wt.%	Pyroxen ABC_2O_6	ABO_3	$\text{Ca}_{1-x}\text{Fe}_{x+y}\text{Ta}_{0.8-2/5y}\text{O}_3$	$\text{FeTa}_{0.8}\text{O}_3$	$\text{Fe}_{1+x}\text{Ta}_{2-2/5x}\text{O}_6$	$\text{Fe}(\text{Fe}_{2-5/3y})\text{Ta}_y\text{O}_4$	
Fe	1.9	44.0	16.7	7.9	19.8	14.0	51.8
Ca	5.0	19.3	14.7	10.9	0.34	0.4	0.33
Si	13.2	23.2	17.3	0.7	0.62	0.3	0.49
Al	0.78	17.3	2.0	0.1	0.12	0.1	1.14
Ta	0.07	6.6	13.4	59.2	58.2	66.9	22.7
O	31.4	44.2	35.1	20.6	19.5	19.3	21.6
Total	n.a.	n.a.	99.1	99.4	98.5	100.9	98.1
Data type	Min.–Max.	Ave.	Ave.	Ave.	Ave.	Ave.	Ave.
N	128	10	23	single spot	4	9	
RD Al	n.a.	n.a.	2.0	n.a.	n.a.	n.a.	n.a.
RD Si	n.a.	n.a.	17.3	n.a.	n.a.	n.a.	n.a.
RD Ca	n.a.	n.a.	14.7	1.00	n.a.	n.a.	n.a.
RD Fe	n.a.	n.a.	16.7	6.5	n.a.	7.2	6.1
RD Ta	n.a.	n.a.	13.4	1.6	n.a.	1.8	19.9
Occurrence		50 °C	50, 200 °C	300 °C	300 °C	300 °C	

In all samples, the highest concentrations of Ta are in oxides of perovskite, tantalite and, most probably, magnetite spinel type. In the slowly and moderately rapidly cooled samples (50 °C/h and 200 °C/h), these oxides are significantly enriched in calcium (Ca) (Figure 9).

The compositions of the oxides with respect to the ratio of Taal + Fe lie on a line which is spanned by the compounds FeTa_2O_6 (tantalite(Fe)— $\text{FeTa}_{0.8}\text{O}_3$ (Ta-perovskite)— Fe_3O_4 (magnetite) in the case of the rather rapidly cooled sample (300 °C/h, S300). In contrast, the calcium-rich Ta iron oxides of the slower-cooled samples (50 °C/h and 200 °C/h) are in a range that has as its starting point the compound $\text{Ca}_{0.5}\text{Fe}_{0.5}\text{Ta}_2\text{O}_6$ and can be expanded to a general perovskite-like compound $\text{Ca}_{1-x}\text{Fe}_{x+y}\text{Ta}_{0.8-2/5y}\text{O}_3$ (Figure 9). The crystals of Ta-oxide in the sample 200 °C/h (S200) were extremely small, so only two measurements could be used.

No concentrations were measured in a concentration range between 30 and 55 wt.% Ta. The silicon-free oxides with $[\text{Ta}] < 30$ wt.% (towards magnetite) were found only in the relatively rapidly cooled sample (300 °C/h). Therefore, the cooling rate seems to play a major role with a kind of turnover point somewhere between 200 °C/h and 300 °C/h. In the relatively slowly cooled sample 50 °C/h, a silicon-containing Ta-rich oxide was found.

In all three samples, a siliceous matrix occurs, whose composition is most comparable to hedenbergite—or an augite without Mg, alkalis and Ti. The hedenbergite could also be written in the form of the augite formula $(Ca, Fe^{II})(Fe^{II}, Al, Ta)(Si, Al)_2O_6$, with the assumption that Fe^{II} can also sit on the first crystal position. The Ta contents in this compound, which in all probability is both crystalline and amorphous (see Figure 7), are very variable and range from near zero to almost 7 wt.%. When plotting Al + Fe, Ca + Fe and Ta, a distinct multilinear correlation is noticeable (Figure 10, right).

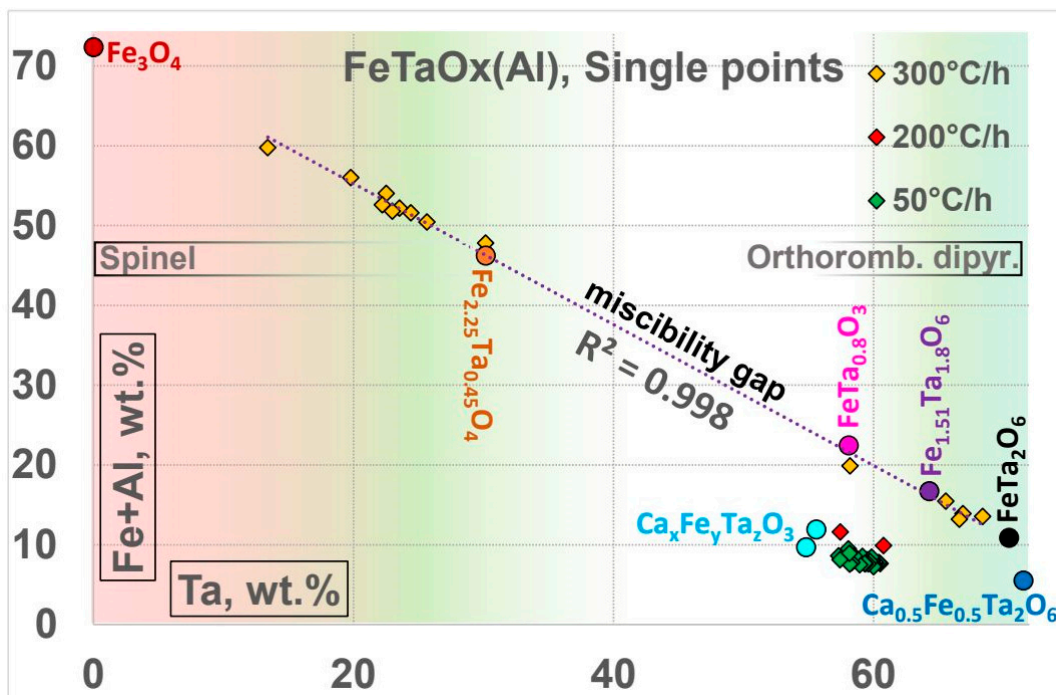


Figure 9. Ratio of Ta: Fe + Al for the three SFS. Explanations in the text. For a better understanding, theoretical Ca-Fe-Ta-oxide compositions are plotted near the measurement points. Detailed data set see Appendix A, Table A1.

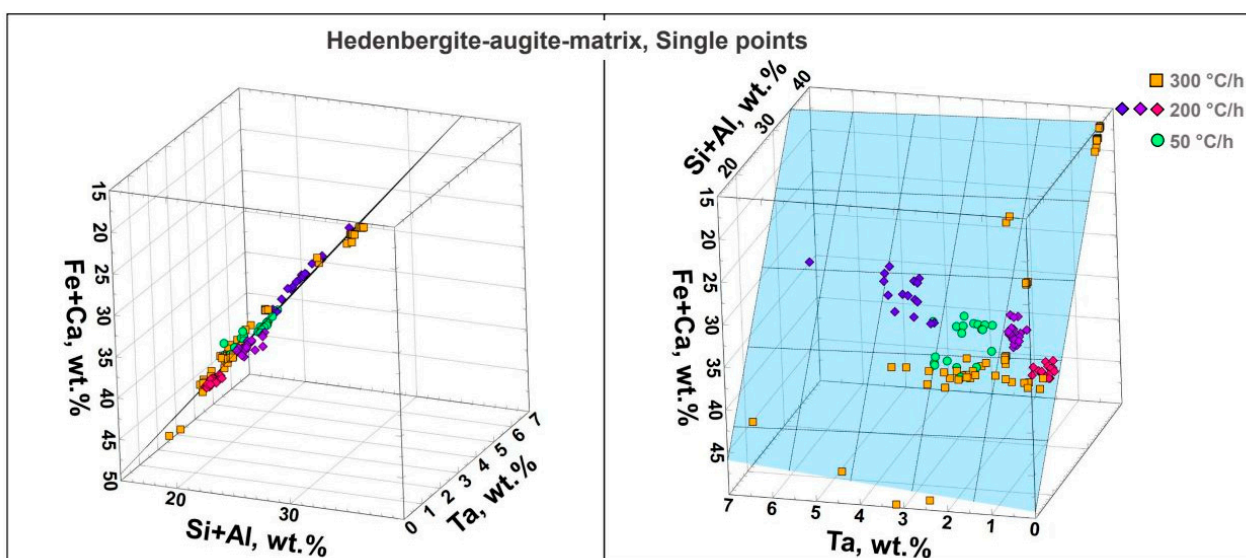


Figure 10. Box plots of Al + Fe, Ca + Fe and Ta, showing a distinct multilinear correlation plane with clustering of Ta-values at 200 °C/h. Further descriptions see text. For detailed dataset, see Appendix A, Table A2.

Remarkably, at 300 °C/h, there is a much larger spread of Ta concentrations between ~0 and 7 wt.%. Interestingly, composition clusters with [Ta] < 1 wt.% (red diamonds), 1–2 wt.% (purple diamonds) and 3–4 wt.% (blue diamonds) occur at 200 °C/h, especially with respect to Ta. In addition, there seems to be a weak positive correlation between the concentration of Ta and Fe + Ca in this sample. The Ta concentrations measured at 50 °C/h range between 1 and 3 wt.% and have the lowest spread.

The other oxides and silicates play only a minor role in the Ta distribution in the samples, especially if they occur as the main component, such as fayalite at 50 °C/h or spinel at 200 °C/h.

4.5. Estimation of Phase Composition and Ta Balancing

The assessment of phase compositions must be considered with some caution, since almost all compounds are variable solid solutions; therefore, it is difficult to determine an average value for the estimation of the semi-quantitative phase composition. In addition, all slag samples are very heterogeneous. For the semiquantitative calculations, initial concentrations of the compounds obtained with PRDA were first determined using the “reference intensity ratio” (RIR) method (e.g., [101]). Based on these concentrations, new concentrations were iteratively determined using the averaged concentrations of the detected compounds measured with EPMA and the bulk composition of the sample, with the goal of complete elemental balance (Equation (4), especially for Ta) and optimizing the total sum of all compounds/phases considered (Equation (2)):

$$R_{EI}(\text{wt.}\%) = \text{CEl}_{\text{init}}(\text{wt.}\%) - \sum \text{CEl}_{\text{Phases}}(\text{wt.}\%) \times C_{\text{Phase}}(\text{wt.}\%) \times F = \min \quad (4)$$

$$[100(\text{wt.}\%) - \sum \text{Phases}(\text{wt.}\%)](\text{abs}) = \Delta(\text{abs}) = \min \quad (5)$$

R_{EI} = rest of the element concentration after subtraction of all partial concentration portions of phases; CEl_{init} = measured bulk concentration; $\text{CEl}_{\text{Phase}}$ = concentration of element in the phases of interest; C_{Phase} = element concentration in the phase; F = optional factor if the element has to be assigned to more than one phase.

An enrichment factor for Ta was then determined from these results. Due to the high variability of the Ta compounds (hedenbergite/augite, tantalite/perovskite, spinel), no feasible semi-quantitative phase composition could be estimated for 300 °C/h. The results of the estimation are presented in Figure 11.

The estimation shows that in the case of the 200 °C/h (S200) sample, most of the Ta (~75%) is in the hedenbergitic matrix (58 wt.%). Other important components are spinel (magnetitic), hematite, fayalite and Fe_{1-x}O . The Ta oxide accounts for only 0.1 wt.%. Therefore, most of the Ta, 75%, is bound in the matrix and only 14% in Ta-oxide. The enrichment factor, however, is highest for Ta in Ta-ox (99%) since the proportion of the compound in the phase composition is included here.

The phase composition of the 50 °C/h sample (S50) is dominated by fayalite (52 wt.%). The hedenbergitic matrix is represented by only 17 wt.%. Other important compounds are hercynitic spinel, Fe_{1-x}O and Fe. The Ta-rich compounds Ta-Ox and Ta-SilicoOx are represented with only 0.4 and 0.3 wt.%. Due to the large mass, most of the Ta in this sample is also bound in the matrix (57%). The Ta-Ox contains 27% and the Ta-SilicoOx 9% of the Ta. The enrichment factor for the Ta-Ox here is 77% next to Ta-SilicoOx with 18% and the hedenbergitic matrix with 3%. For sample S50, a proportion of Fe was found, which can be regarded as normative and must be attributed to the high inhomogeneity of the samples. However, the influence on the balancing of Ta should be rather limited due to the only small residual error from the balancing between the phases used and the assigned elements (except Fe) of 0.26 wt.%.

Overall, it can be seen that the Fe^{III} -containing compounds in the faster cooled sample (S200) have a lower $\text{Fe}^{\text{II}}/\text{Fe}^{\text{III}}$ (\rightarrow more Fe^{III} , see Appendix A, Table A3) compared to the slower cooled sample (S50).

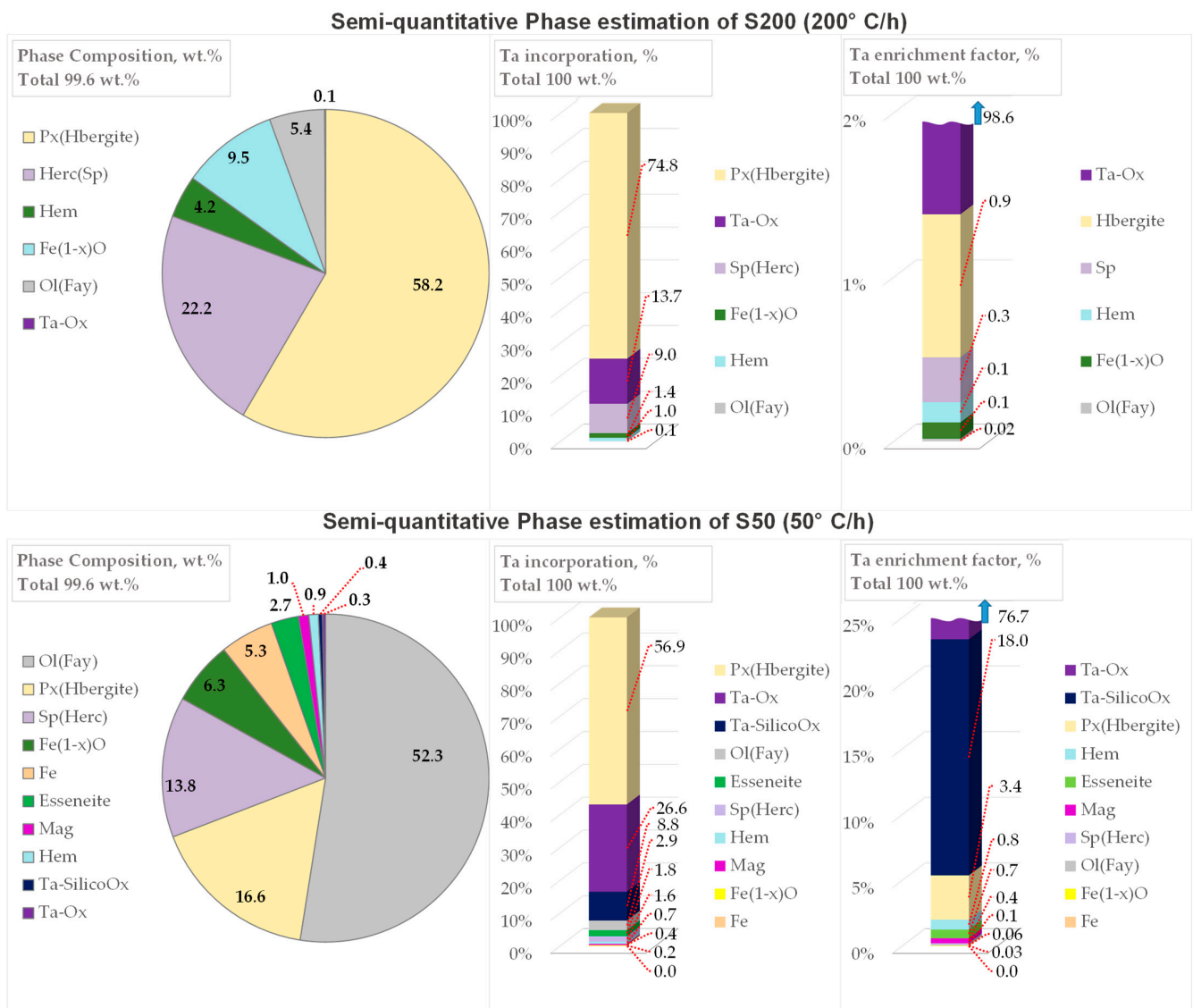


Figure 11. Semi-quantitative phase composition, Ta incorporation and Ta enrichment factor of two SFS. Above (200 °C/h): Hbergite: hedenbergitic matrix, Sp: spinel, Hem: hematite, Ta-Ox: Ta-rich oxide. Below (50 °C/h): Hbergite: hedenbergitic matrix, Herc: hercynitic spinel, Mag: magnetite, Hem: hematite, Ta-SilicoOx: perovskite-like silicon containing Ta-oxide of type ABO_3 , Ta-Ox: Ta-rich oxide.

5. Discussion

In this work, the EnAM approach was applied for the recovery of Ta from slags originating from waste processing of containing Ta-bearing scrap. One of the first steps to apply this approach is the development of a suitable slag system and the investigation of the incorporation of Ta into the compounds formed during solidification. This article concentrates on the incorporation of Ta into the different slag compounds.

5.1. Speciation Analysis of Ta and Fe

The performed speciation of iron in the slags gives semi-quantitative information about the formal oxidation states and the amount of the basic components fitted into the slag spectra. The determined amounts of Fe^{II} and Fe^{III} are based on the standard materials olivine and magnetite that were incorporated in the best fits. The corresponding results and the visible trend for the formation of Fe^{III} with higher cooling rates (Table 2) are in good agreement with the results obtained from PXRD, EPMA and the simulations. However, the standard materials used for the iron speciation cannot entirely describe the spectra of

S200 and S50—especially at the pre-edge peak and in the post-edge region. This is also indicated by the residuals plotted in Appendix A, Figure A1. Since the post-edge region is highly sensitive to the atomic environment of the absorbing atom, it is likely that at least one additional compound contributes to the spectra. Investigations with EPMA and PXRD showed that, e.g., kirschsteinite, hercynite and hedenbergite are present as additional iron bearing phases. The fit results of the XANES spectra may be further improvable by using these compounds as standard materials. This approach would require the synthesis of these mineralogical compounds, since they are barely available in a natural form that has a sufficient pureness.

The low-Ta slags S50, S200 and S300 ([Ta] = 0.8 wt.%) showed only weak signals at approx. 9886 eV in the recorded Ta L_{III}-edge XANES spectra (Appendix A, Figure A2), which are not strong enough for sensible normalization and evaluation. Therefore, high-Ta slags (HS50 and HS300) containing a Ta content of approx. 10 wt.% (necessary to be well above the detection limits) had to be specifically synthesized and investigated. As seen in Section 4.2, the comparison of the XANES spectra recorded at the Ta L_{III}-edge showed that tantalum is most likely present as Ta^V species. This result is further confirmed by additional XANES spectroscopy at the Ta L_I-edge, which probes 2s to 5p transitions. The energy shifts of the edge position in the slag spectra are similar to those for Ta₂O₅ and tantalite (Appendix A, Figure A3). This is consistent with the results of Burnham et al., who found within their investigations regarding synthetic glasses of mineral melts that tantalum is present as Ta^V even under different oxygen fugacities [97]. It is plausible that the oxidation state of Ta in the samples S50, S200 and S300 can be expected to be +V, even though the Ta contents in these slags are approx. ten times lower compared to the high-Ta slags. Since the process parameters during the synthesis remained the same, similar formation conditions with similar influences on the species can be assumed.

5.2. Behavior of the Selected Slag System

During the generation of the fayalitic slag, there are two behaviors to take into account; the first one is the reaction between Fe⁰ and hematite (Equation (1)) and the second one is the diffusion of oxygen from the crucible surface to reach the metal (Equations (4)–(6)), which due to its density at the bottom of the crucible. The simulations showed that pO₂ from 10^{−8} to 10^{−11} bar is needed to obtain the different experimental results.



The high-temperature residence time proved to be adequate to form a fully liquid slag, as the speciation results in Table 2 show a high amount of Fe^{II}, modeling 80% dissolution according to Figure 1a. Since the temperature chosen was 1350 °C, the slower the cooling rate, the more time the system will have to continue the reaction of Equation (1) until at least 800–900 °C, where the oxygen diffusion will be too low to continue. The reaction between Fe⁰ and O₂ is much slower due to the lower partial pressures in the system. A combination of Fe^{II} and Fe^{III} allows the promotion of spinel formation during the solidification stage, freeing the silica to react with other elements such as Ca or even Ta. For this particular case, a slower cooling rate gave more time to increase Fe^{II} production at high temperature, causing the silica to seek combination with iron to form fayalite. As shown in Figure 1b, the higher the dissolution of Fe, the higher the olivine content and the lower the formation of spinels and pyroxenes, in full agreement with the results described in Section 4.4.2.

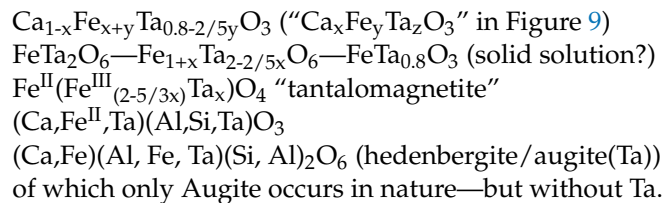
5.3. Ta Compounds Discovered in the SFS

For an initial assessment of the behavior of the element, it is helpful to consider the pre-dominant speciation, the possible coordinations, and the ion radii in the various coordinations.

In nature, Ta occurs exclusively as Ta^V. This was also confirmed for the samples of this study via XANES results. It can be 6-, 7- and 8-coordinated and has ionic crystal radii of 0.78, 0.83 and 0.88 [59]. Thus, it is, on the one hand, not possible that this element is incorporated in silicates instead of, e.g., Al in the tetrahedral position of Si (0.4, [59]). On the other hand, it has similar ionic radii to Fe^{II}, Fe^{III} and Ti^{IV} [59]. Therefore, it is plausible that it can represent these elements in suitable compounds (see Section 2.3).

Considering the natural analogues presented in Section 2.3, the following compounds are interesting: ABO₃ represented by CaTiO₃ and FeTiO₃, AB₂O₆ represented by FeTa₂O₆, AB₂O₄ represented by magnetite/hercynite (solid solution) and ABC₂O₆ represented by hedenbergite/augite (clinopyroxene).

Based on these base structures, taking into account the incorporation of Ta and the identified chemistry using EPMA single spot analysis, the following compounds are initially conceivable:



The other compounds not described so far, derived from perovskite, tantalite or magnetite are plausible but hypothetical. In the following, the plausibility of these hypothetical compounds is discussed based on the original compounds and considering the ionic radii and the measured EPMA data.

The proof that Ca also occurs in XTa₂O₆ is provided by rynersonite, which crystallizes in the same crystal system as tantalite [65]. However, a description of a solid solution tantalite—rynersonite—was not found in the literature.

There is also a natural analog that could help to assess the incorporation of Ta in magnetite: titanomagnetite (see Section 2.3), which has a spinel structure. Here, too, it is plausible to assume a hypothetical tantalomagnetite Fe^{II}(Fe^{III}_{(2-5)/3x}Ta_x)O₄ due to the similar ionic radii of Ti^{IV} and Ta^V. The Ta-containing magnetite with the maximum Ta content (30.2 wt.%) calculated in Figure 9 corresponds to a stoichiometric factor of 0.45 (Fe(Ta_{0.45}Fe_{1.25})_{1.7}O₄). This is lower than the maximum possible stoichiometric factor in titanomagnetite (see Section 2.3). The same could be true for the incorporation of Ta into ilmenite to form a hypothetical Tantaloilmenite (FeTa_{0.8}O₃). In this trigonal compound, Ti^{IV} is octahedrally coordinated what—in principle—should also be plausible for Ta^V.

In orthorhombic perovskite CaTiO₃, Ca is 8-fold and Ti octahedrally coordinated [82]. Replacement of Ti^{IV} with Ta^V in the latter coordination site is plausible due to the very similar ion radius and the similar charge number of Ti^{IV} and Ta^V.

An assessment of whether a hypothetical compound FeTa_{0.8}O₃ in the studied samples has an ilmenitic or perovskitic structure could not be obtained from the PRDA results of the very complex and poorly crystalline synthetic slag samples in combination with low Ta bulk concentration. If a solid solution is established between orthorhombic tantalite/rynersonite ((Ca,Fe)Ta₂O₆) and FeTa_{0.8}O₃ or Ca_{1-x}Fe_{x+y}Ta_{0.8-2/5y}O₃, respectively (see Figure 9), the assumption that these compounds are similarly structured as orthorhombic perovskite is plausible.

The silicon containing Ta-rich compound (Ta-SilicoOx in Figure 11, column "ABO₃" in Table 3) in the SFS 50 °C/h (S50) cannot be a silicate in the strict sense since Ta cannot be tetrahedrally coordinated (see Section 2.3). Therefore, it is rather an oxide, which can most likely be derived from the formula CaTa_{0.8}O₃, (analog to CaTiO₃) where Fe can additionally be assigned to the Ca position and Al and Si to the Ta position. To balance the stoichiometric formula, Ta must occupy both the first and second cation positions. An exchange of Ca^{II} for Ta^V in the first cation position would fit from the perspective of the ionic radius (see, e.g., [59]), but the charge number is very different (2+ vs. 5+). However, in the simple

Ta-containing oxide ixiolite (see Section 2.3), Ta sits on the same crystal position as the low-charged Fe^{II} , so that an exchange of Ca for Ta would at least be plausible.

The only true silicate compound in the SFS that incorporates Ta is a pyroxene or pyroxenitic glass. The multilinear correlation shown in Figure 10 indicates that the Ta concentration could have a mediating function between the concentration sums $\text{Fe} + \text{Ca}$ (wt.%) and $\text{Al} + \text{Si}$ (wt.%). If the formula is grouped like $(\text{Ca—Fe}(\text{Al,Fe})\text{Al—Si})\text{O}_6$, the probability is that Ta is incorporated into the middle subgroup: “ $\text{Fe}(\text{Al, Fe, Ta})\text{Al}$ ”. This would confirm the observation that Ta behaves similarly to Ti during solidification and is incorporated in hedenbergitic/augitic (crystalline and/or amorphous) pyroxene with the general formula ABC_2O_6 in the B position together with elements such as Fe and Al in octahedral coordination.

5.4. Relationships between Ta Compounds

The studies on synthetic slags with different cooling temperatures show a very variable behavior of Ta. Here, a change in incorporation strategy appears to be present between the 200 °C/h and 300 °C/h cooling rates. The iron-rich but calcium-poor oxides (Section 4.4.2, Figure 9) observed at rapid cooling (300 °C/h) appear to form a solid solution with FeTa_2O_6 and Fe_3O_4 end members. Due to the different crystal systems (Fe_3O_4 : spinel vs. FeTa_2O_6 : orthorhombic), it is unlikely that this solid solution is complete. Similarly, it is plausible that, especially on the Fe_3O_4 side of the system, these oxides do not incorporate Ca, since this has a very large ionic radius for incorporation into the spinel structure. Interestingly, the oxides on the FeTa_2O_6 side also hardly incorporate Ca in this sample.

In the slower cooled samples (<200 °C/h), similar oxides of the type $\text{Ca}_x\text{Fe}_y\text{Ta}_z\text{O}_6$ are formed, whereby, here, considerable amounts of Ca as well as Fe are present. In addition, there seems to be a possible negative relationship between the cooling rate and the Ca content of the Ta oxides (Figure 9). The iron-rich region towards Fe_3O_4 is missing. Due to the incorporation of Ca into the crystal structure, this is plausible for the reasons already mentioned above. With slow cooling, another compound with a complex chemical composition (ABO_3 with A: Ca, Fe^{II} , Ta; B: Al, Si, Ta) appears. This indicates that a sequence exists with respect to the rapidity of cooling. If the cooling rate is fast, the formation of iron-rich oxides—especially a spinel similar to titanomagnetite—seems to be favored. If the cooling rate decreases, additional Ca is incorporated into the Ta-rich oxides, inhibiting spinel formation and favoring perovskite as primary Ta-compound. With relatively slow cooling, additional complex perovskite-like oxides with Al, Si, Ca, Fe and Ta are formed.

All samples contain a siliceous matrix of pyroxenitic composition similar to hedenbergite/augite. This Ta-containing silicate present in the matrix does not play such a major role in terms of Ta enrichment, but it does contain a large proportion of the Ta due to its high absolute content. Regarding the PXRD results, this component is crystalline to a considerable extent. This means that even a rapid cooling rate of 300 °C/h cannot yet be described as quenching with the formation of high proportions of amorphous phase and low crystalline content. This silicate compound can incorporate Ta to a limited extent (max. 6–7 wt.% Ta, Figure 10). The distribution of Ta at the various cooling rates indicates that the faster this proceeds the higher the variance in Ta concentrations becomes. Cluster formation also occurs, which indicates a very heterogeneous composition of the melt.

5.5. Assessment of Potential Engineered Artificial Minerals, Ta-EnAMs

The real motivation for studying the behavior of Ta in slag is to find an efficient enrichment process in form of a EnAM to separate the Ta as completely as possible while minimizing the mass to be processed: $[\text{Ta}]_{\text{EnAM}}/[\text{Ta}]_{\text{Matrix}} = \max$ and $M(\text{EnAM}_{(\text{Ta})}) = \min$. This would be fulfilled by a compound containing maximum high concentrations of Ta and quantitatively scavenging Ta from the molten slag. The best candidate would be Ta_2O_5 (81.9 wt.% Ta), which, however, does not form in the slags containing Fe and Ca. The best option, therefore, are tantalite- or perovskite-type oxides, which can contain up to 60 wt.% Ta.

Thus, the first step in developing an EnAM-based treatment of slag is to identify potential EnAMs.

The experiments show that with slow cooling (50 °C/h) more complex perovskite-like oxides with Ca, Fe and Ta or Al, Si, Ca, Fe and Ta are formed, the first ones being much more frequent and reaching higher Ta concentrations. Due to the lower calculated percentage of hedenbergitic matrix, a higher percentage of Ta is incorporated into these oxides (26.57 + 8.77 wt.% compared with 8.96 wt.%, Figure 11) than at a higher cooling rate (200 °C/h).

At a high cooling rate of 300 °C/h, significant amounts of Ta are incorporated into titanomagnetite-like spinels (tantalomagnetite) in addition to FeTa₂O₆. A semiquantitative estimation was not possible due to the highly variable solid solution of the titanomagnetite-like spinels (tantalomagnetite), but a major amount of Ta seems to be incorporated in this compound. Unfortunately, the maximum achievable concentrations of Ta are much lower than in the tantalite- and perovskite-type oxides and are at a maximum of 30 wt.% Ta. In addition, this component is not present separately but forms a solid solution with Fe₃O₄, which, in case of a separation, offers the possibility to recover the entire magnetite–tantalomagnetite fraction as a concentrate.

According to the semi-quantitative evaluations of Ta enrichment, a very efficient EnAM is a perovskitic oxide ABO₃, which is preferentially formed in the slower cooled slags. However, this oxide has the disadvantage that it also incorporates Ca in addition to Fe and contains impurities of Al and Si. With this slow cooling, the matrix also seems to be slightly less enriched in Ta, but another disadvantage is the formation of another complex perovskite-like oxide with Al, Si, Ca, Fe and Ta.

If the slag is cooled down faster, a titanomagnetite-like oxide (tantalomagnetite) unfortunately forms a solid solution with Fe₃O₄, which is predominant, although the FeTa₂O₆ crystals discovered there would be the most optimal EnAM, since it contains almost only Fe besides Ta.

At the present time, it seems advantageous to develop a slower cooling rate at which there is a maximum crystal growth rate of the perovskite-type oxide at a minimum nucleation rate. In addition, the incorporation of Ta into the matrix could be minimized using this approach.

6. Conclusions

The thermodynamic simulation of the fayalitic system studied in this work can predict the formation of specific compounds, such as pyroxene, olivine, and spinel, which were detected in the real samples, especially with a slow cooling rate. However, the software database is limited in detail when speciation and different classes of minerals are present, which is exactly the case in this complex system. Improvements in the simulation may be achieved in future works once the configuration of the system has been more comprehensively evaluated.

The performed XANES measurements and analyses of the recorded spectra gave direct information about the speciation of iron and tantalum in the slags. It was found that the iron species change with different cooling rates. For 50 °C/h and 200 °C/h Fe^{II} dominates, a cooling rate of 300 °C/h led to a highly increased amount of Fe^{III}. In agreement with calculated models for the low-Ta slags, the species of tantalum was found to be Ta^V — although this result from XANES spectroscopy is only based on the high-Ta slags. In total, the findings confirm the results obtained from PXRD and EPMA with which the phase composition of the bulk and single grains were examined.

This study shows that the investigation of slags by means of XANES spectroscopy is an eminently valuable method for determining the contained species of tantalum and iron. Depending on the evaluation procedure, qualitative as well as semi-quantitative information is provided, which enhances the understanding of phase formation and supports the development of mineralogical models. Especially with laboratory-based X-ray absorption fine structure (XAFS) spectrometry, the experimental studies are easily accessible in contrast

to investigations at a synchrotron facility. However, the lab applications are limited if, e.g., the element content in the sample is low or information about the spatial distribution requiring an optical resolution in the micrometer range is of interest. This aspect applies for tantalum since the target concentration in the bulk sample is below 1 wt.% and the incorporation of tantalum is not equally distributed. Thus, μ -XANES spectroscopy with which the grains containing up to 60 wt.% Ta can be examined is a promising option for an additional confirmation of the results obtained so far.

The applied cooling rates in the fayalitic slag system play a significant role, with a transition of formation from perovskitic to tantalitic—tantalomagnetite oxides taking place in the range between 200 and 300 °C/h. As long as the EnAMs have been found, the next step is the refinement of the slag system and the cooling curves. In order to specify the response of Ta in the studied slag system, further experiments with slower cooling rates (<50 °C/h) should be performed. To verify the comparable behavior of Ti and Ta, syntheses (e.g., sol–gel syntheses) with magnetite–tantalomagnetite stoichiometry could be performed. The same applies to the verification of the incorporation of Ca into tantalites and the formation of silicon-containing perovskite-like oxides. In this context, the development of a thermodynamic database with Ta-containing mineral phases represents an important step in designing the synthetic slag system for maximizing the incorporation of Ta into the desired EnAM.

A current challenge involves preventing the incorporation of Ta into the pyroxenitic component contained in the matrix. Although promising EnAMs have already been discovered, most of the Ta remains bound in the matrix of the slag. The studies show, for the first time, that Ta in synthetic slag behaves similarly to Ti and therefore accumulates in corresponding perovskite-, spinel- or silicate-like compounds. These oxides are the most promising EnAMs. In addition, oxides can also be found that have a direct counterpart in nature, such as FeTa_2O_6 (Tantalite(Fe)).

In conclusion, the future direction of this research involves the assessment of several critical questions that will shape the perspectives of this work. Firstly, the efficiency of separating perovskite-type oxides must be assessed since Ta was mostly concentrated in this phase. Secondly, an investigation is required to determine whether processing methods for perovskite-type oxides can effectively capture the more complex silicon-containing perovskitic oxide, potentially advancing this approach. Thirdly, the potential challenges posed by contaminants introduced during beneficiation, especially concerning the silicon content, need to be examined to refine hydrometallurgical processing strategies. Additionally, the feasibility of liberating and separating the titanomagnetite-like spinel (tantalomagnetite) at the rims of Fe_3O_4 crystals might be promising and should be explored. Moreover, methods must be developed to simultaneously separate tantalomagnetite-like spinel and FeTa_2O_6 from the slag, which presents an intriguing field for research.

Author Contributions: Conceptualization, T.S.; funding acquisition, B.F.; investigation, T.S., J.H., J.W., D.M., H.L., U.E.A.F. and B.F.; methodology, J.H., J.W., D.M., H.L., U.E.A.F. and B.F.; project administration, B.F.; supervision, T.S., U.E.A.F. and B.F.; visualization, T.S., J.H., J.W., D.M. and H.L.; writing—original draft, T.S., J.H., J.W., D.M. and H.L.; writing—review and editing, T.S., J.H., J.W., D.M., H.L., U.E.A.F. and B.F. All authors have read and agreed to the published version of the manuscript.

Funding: This research was funded by the German Research Foundation (DFG) within the scope of the priority program “Engineered Artificial Minerals (EnAM)—a geo-metallurgical tool to recycle critical elements from waste streams” (SPP2315).

Data Availability Statement: Data is part of ongoing research and will be only available on request.

Acknowledgments: The authors acknowledge the financial support of the German Research Foundation within the priority program “Engineered Artificial Minerals (EnAM)—a geo-metallurgical tool to recycle critical elements from waste streams” (SPP 2315, Grant No. 470553874). We additionally acknowledge the support of the Open Access Publishing Fund of the Clausthal University of Technology.

We thank Petra Sommer, Heike Grosse and Maike Gamenik from the Institute of Mineral and Waste Processing, Waste Disposal and Geomechanics for their analysis.

Conflicts of Interest: The authors declare no conflicts of interest. The funders had no role in the design of the study; in the collection, analyses, or interpretation of data; in the writing of the manuscript; or in the decision to publish the results.

Appendix A

Table A1. Data used to plot Figure 9.

wt. %	Fe	Ca	Si	Al	Ta	O	Total
300 °C/h	13.5	0.297	0.257	0.062	68.4	19.5	102.0
	13.8	0.42	0.503	0.102	66.9	19.6	101.3
	13.2	0.296	0.225	0.064	66.6	18.9	99.3
	15.4	0.499	0.229	0.043	65.6	19.4	101.2
	19.8	0.337	0.618	0.119	58.2	19.5	98.5
	47.3	0.349	0.549	0.571	30.2	21.5	100.4
	49.7	0.347	0.215	0.784	25.6	21.0	97.6
	50.8	0.327	0.217	0.79	24.4	21.0	97.6
	51.4	0.369	0.78	0.794	23.5	21.7	98.5
	51.0	0.484	0.436	0.809	23.0	21.1	96.8
	53.0	0.232	0.508	1.057	22.5	21.8	99.1
	50.5	0.336	0.6	2.144	22.2	22.1	97.9
	54.1	0.333	0.615	1.917	19.8	22.4	99.2
	58.4	0.196	0.461	1.404	13.4	21.5	95.4
200 °C/h	9.7	11.01	0.355	0.184	60.8	21.2	103.2
	10.5	11.45	0.671	1.109	57.5	22.0	103.2
50 °C/h	7.5	10.8	0.606	0.098	60.5	20.6	100.2
	7.7	10.8	0.334	0.125	60.4	20.4	99.7
	7.6	10.8	0.458	0.11	60.2	20.4	99.5
	7.7	10.8	0.365	0.121	60.1	20.4	99.5
	7.5	10.7	0.629	0.084	60.0	20.5	99.4
	7.9	10.9	0.454	0.119	59.9	20.5	99.7
	8.0	11.0	1.279	0.128	59.6	21.4	101.4
	7.8	10.9	1.246	0.1	59.5	21.3	100.8
	8.3	10.9	0.625	0.21	59.1	20.7	99.9
	9.3	11.0	1.228	0.176	58.1	21.5	101.2
	8.4	11.2	1.659	0.188	57.3	21.6	100.4
	7.2	10.8	0.318	0.092	60.0	20.1	98.4
	8.4	10.9	0.687	0.089	59.8	20.8	100.7
	7.9	10.9	0.247	0.094	59.7	20.2	99.0
	7.5	10.9	0.458	0.103	59.6	20.3	98.9
	7.5	11.0	0.622	0.146	59.4	20.5	99.0
	7.5	11.0	0.396	0.176	59.3	20.3	98.6
	7.3	11.0	0.577	0.154	58.9	20.3	98.3
	8.4	10.9	0.74	0.182	58.5	20.7	99.5
	7.6	11.0	0.733	0.149	58.3	20.4	98.3
7.4	11.1	0.598	0.203	58.2	20.3	97.7	
8.7	10.9	0.784	0.227	58.2	20.8	99.6	
8.0	11.1	0.474	0.12	57.4	20.1	97.2	

Table A2. Data used to plot Figure 10.

wt. %	Fe	Ca	Si	Al	Ta	O	Total
300 °C/h	33.0	9.6	14.7	2.69	6.61	34.0	100.6
	39.7	6.9	14.0	1.60	4.44	32.5	99.1
	23.1	13.8	18.4	2.48	3.67	36.2	97.6
	42.5	5.5	13.6	0.78	3.49	31.4	97.2
	22.7	14.1	18.6	2.39	3.35	36.2	97.3
	42.6	7.1	13.5	1.63	3.18	32.6	100.5
	24.2	12.9	18.9	2.18	2.84	36.2	97.1
	23.7	14.5	17.9	2.42	2.82	35.9	97.3
	22.9	14.2	18.5	2.43	2.48	36.1	96.6
	44.0	5.0	13.2	2.14	2.43	32.1	98.9
	23.8	14.6	17.8	2.39	2.41	35.7	96.7
	23.3	14.4	18.1	2.88	2.36	36.3	97.3
	24.2	12.8	19.0	2.24	2.22	36.3	96.7
	23.7	14.1	18.8	2.60	2.18	36.8	98.2
	23.3	14.4	18.4	2.50	2.15	36.2	97.0
	22.9	14.6	18.3	3.07	2.10	36.5	97.4
	22.3	13.9	18.6	4.07	2.10	37.3	98.1
	22.9	14.5	18.5	2.97	2.02	36.6	97.6
	23.3	14.3	18.4	2.81	1.99	36.4	97.2
	23.5	14.3	18.5	2.86	1.93	36.6	97.7
	22.6	14.5	18.8	3.07	1.90	36.9	97.9
	24.6	12.7	19.0	2.33	1.80	36.4	96.9
	22.6	14.2	18.6	3.87	1.75	37.3	98.3
	15.9	8.2	23.0	7.43	1.74	41.1	97.3
	15.1	8.2	23.2	7.22	1.66	40.9	96.3
	23.1	13.4	18.7	3.88	1.66	37.2	98.0
	24.5	13.1	19.0	3.19	1.42	37.2	98.5
	21.5	14.5	18.6	4.41	1.26	37.5	97.7
	21.4	14.5	18.7	4.54	1.25	37.7	98.1
	21.1	14.8	18.8	4.48	1.25	37.7	98.1
	21.5	14.6	18.5	4.35	1.24	37.3	97.5
	21.8	14.7	18.5	4.37	1.23	37.4	98.0
	26.0	11.6	19.4	2.11	1.13	36.4	96.7
	9.7	19.3	20.7	5.99	1.02	39.7	96.4
	10.0	19.2	20.9	5.79	1.02	39.8	96.7
	9.8	19.3	20.9	5.82	1.01	39.8	96.7
	10.0	19.2	20.8	5.93	1.01	39.8	96.7
	9.7	19.3	21.0	5.95	1.00	40.1	97.0
	26.1	11.9	19.6	2.11	1.00	36.7	97.4
	21.9	15.9	16.9	4.66	0.71	36.2	96.3
	26.3	11.6	19.8	2.00	0.62	36.8	97.1
	22.5	15.8	16.6	4.74	0.61	36.1	96.4
	31.0	7.7	20.0	1.92	0.38	36.7	97.7
	25.4	12.1	20.3	1.80	0.32	37.1	97.0
	4.3	13.4	20.8	15.23	0.09	44.0	97.8
	4.6	13.3	21.1	14.57	0.09	43.7	97.3
	1.9	13.8	19.7	17.25	0.08	43.9	96.6
	3.0	13.6	20.2	15.90	0.08	43.5	96.3
	2.0	13.7	19.9	17.23	0.08	44.2	97.1
	3.0	13.6	20.2	15.98	0.07	43.7	96.5
	2.0	13.8	19.8	17.24	0.07	44.1	97.0
	3.1	13.5	20.5	15.70	0.07	43.7	96.5
	1.9	13.8	19.7	17.08	0.07	43.8	96.4
	3.0	13.7	20.2	16.16	0.07	43.8	96.9
	2.0	13.7	19.7	17.07	0.07	43.8	96.4
	3.1	13.7	20.2	15.76	0.07	43.5	96.3

Table A2. Cont.

wt. %	Fe	Ca	Si	Al	Ta	O	Total
200 °C/h	16.6	14.1	17.4	7.55	4.05	37.9	97.6
	17.3	14.9	16.6	7.70	3.85	37.7	98.1
	17.0	13.7	17.5	7.76	3.74	38.1	97.7
	17.1	13.6	17.4	7.81	3.61	38.0	97.5
	15.3	14.2	17.7	8.46	3.55	38.7	97.9
	15.4	14.2	17.8	8.27	3.46	38.6	97.7
	17.1	14.0	17.4	7.65	3.45	38.0	97.6
	15.2	14.0	18.0	8.27	3.43	38.7	97.6
	17.7	14.9	16.5	7.63	3.40	37.5	97.7
	17.2	13.9	17.2	7.60	3.36	37.7	97.0
	18.4	14.7	17.0	7.06	3.01	37.5	97.7
	18.6	14.7	17.2	7.20	2.96	38.0	98.6
	14.0	14.2	18.1	8.54	4.14	39.0	98.0
	13.8	14.4	18.0	8.22	5.94	38.9	99.2
	15.3	14.2	17.6	8.11	4.20	38.3	97.6
	15.7	13.3	18.3	8.10	4.24	38.9	98.5
	19.1	14.7	17.3	7.56	1.30	38.2	98.1
	19.2	14.6	17.6	6.93	1.29	38.0	97.5
	19.2	14.8	17.6	7.01	1.27	38.1	98.0
	18.8	14.7	17.9	7.09	1.25	38.3	98.1
	19.4	14.7	17.7	6.88	1.23	38.1	97.9
	20.8	14.7	17.4	7.06	1.17	38.2	99.2
	19.6	14.8	17.6	6.65	1.17	37.9	97.8
	20.2	14.6	17.7	6.27	1.11	37.7	97.5
	19.5	14.8	17.8	6.27	1.10	37.7	97.2
	19.3	14.8	17.8	6.94	1.09	38.3	98.3
	20.4	14.7	17.8	6.54	1.08	38.2	98.7
	19.6	14.8	17.6	7.17	1.06	38.3	98.4
	19.1	14.8	18.2	6.70	1.04	38.4	98.3
	19.7	14.7	17.6	6.42	1.01	37.6	97.1
	19.3	14.8	17.5	8.47	1.28	39.2	100.6
	17.6	15.0	17.9	8.11	1.35	39.0	98.9
	17.9	14.8	18.2	7.95	1.18	39.2	99.1
	19.8	14.2	17.9	7.87	0.96	39.0	99.8
	18.0	14.8	18.4	7.52	1.27	39.1	99.0
	22.2	15.2	18.9	3.55	0.59	37.3	97.7
	21.8	15.2	19.0	3.79	0.47	37.5	97.8
	21.8	15.2	19.0	3.67	0.40	37.5	97.6
	21.9	15.3	19.1	3.56	0.39	37.5	97.8
	22.6	15.2	19.6	3.13	0.31	37.8	98.6
22.3	15.2	19.3	3.26	0.29	37.5	97.8	
22.3	15.2	19.3	3.30	0.24	37.6	98.0	
21.9	15.0	19.2	4.14	0.23	38.0	98.5	
22.1	15.2	19.1	3.55	0.23	37.5	97.7	
22.5	15.1	19.3	3.17	0.22	37.5	97.8	
22.5	15.2	19.5	3.11	0.21	37.7	98.2	
22.0	15.1	19.3	3.77	0.14	37.8	98.2	
21.0	15.4	19.9	4.07	0.23	38.6	99.2	
21.0	15.4	19.7	3.87	0.38	38.3	98.7	
21.5	15.3	20.1	3.43	0.32	38.4	99.1	
21.5	15.3	19.7	3.38	0.62	38.0	98.5	
21.7	15.3	20.1	3.33	0.20	38.4	99.1	
50 °C/h	23.5	14.1	18.6	2.51	2.12	36.3	97.1
	21.8	15.0	18.8	2.92	2.26	36.9	97.7
	21.8	15.0	19.4	2.72	1.83	37.2	98.0
	21.7	14.9	18.7	2.85	2.74	36.7	97.6
	21.6	14.9	18.8	2.99	2.77	36.9	98.0

Table A2. Cont.

wt. %	Fe	Ca	Si	Al	Ta	O	Total
	21.5	14.9	19.1	3.10	2.51	37.3	98.3
	21.0	14.7	19.1	2.62	2.74	36.7	96.9
	19.8	14.9	19.4	2.78	1.48	36.6	95.0
	19.0	15.0	17.4	6.65	2.31	37.7	98.0
	18.5	15.2	17.3	7.41	1.90	38.2	98.5
	18.5	15.2	17.1	7.41	1.87	38.0	98.1
	18.4	15.3	17.4	7.22	2.35	38.2	98.8
	18.4	15.1	16.9	7.54	2.46	38.0	98.4
	18.3	15.1	17.8	6.82	2.32	38.2	98.5
	18.2	15.2	17.0	8.06	1.69	38.3	98.5
	18.2	15.1	17.0	7.95	1.85	38.1	98.2
	17.9	15.4	17.5	7.36	2.00	38.3	98.5
	17.8	15.4	17.2	7.75	2.10	38.3	98.6
	18.0	15.1	17.2	7.28	2.99	38.0	98.6
	17.2	15.3	16.8	8.27	2.33	38.2	98.2

Table A3. Iteratively optimized data used for calculations in Figure 11. The ratio of Fe^{II}/Fe^{III} was calculated using virtual compounds. *: Pure elemental Fe

S50	Al	Ca	Fe ^{II}	Fe ^{III}	O	Si	Ta	Sum
Ol(Fay)	0.03	10.36	41.43	0.00	31.92	13.83	0.04	97.6
Px(Hbergite)	5.10	15.01	12.10	7.82	38.54	18.11	2.24	98.9
Sp(Herc)	22.68	0.00	30.02	13.09	34.40	0.00	0.08	100.3
Fe(1-x)O	0.20	0.15	56.71	18.26	24.51	0.00	0.04	99.9
Fe	0.02	0.15	100.0*	0.00	0.00	0.03	0.00	100.2
Esseneite	17.20	13.59	0.00	3.68	44.60	19.84	0.44	99.4
Mag	0.96	0.15	38.76	33.14	26.54	0.00	0.25	99.8
Hem	2.12	0.00	0.00	68.39	28.63	0.00	0.50	99.6
Ta-SilicoOx	1.64	14.60	16.66	0.00	34.54	17.00	14.09	98.5
Ta-Ox	0.00	10.89	7.99	0.00	20.83	0.81	59.51	100.0

S200	Al	Ca	Fe ^{II}	Fe ^{III}	O	Si	Ta	Sum
Px(Hbergite)	3.93	15.15	21.53	0.00	37.85	19.23	0.54	98.2
Herc(Sp)	3.69	0.12	25.40	40.77	27.90	0.16	0.17	98.2
Hem	0.33	0.20	0.00	69.56	29.58	0.24	0.08	100.0
Fe(1-x)O	0.29	0.14	49.48	24.14	25.70	0.19	0.06	100.0
Ol(Fay)	0.05	12.23	37.91	0.00	32.32	14.22	0.01	96.7
Ta-Ox	0.18	11.01	9.73	0.00	21.19	0.36	60.77	103.2

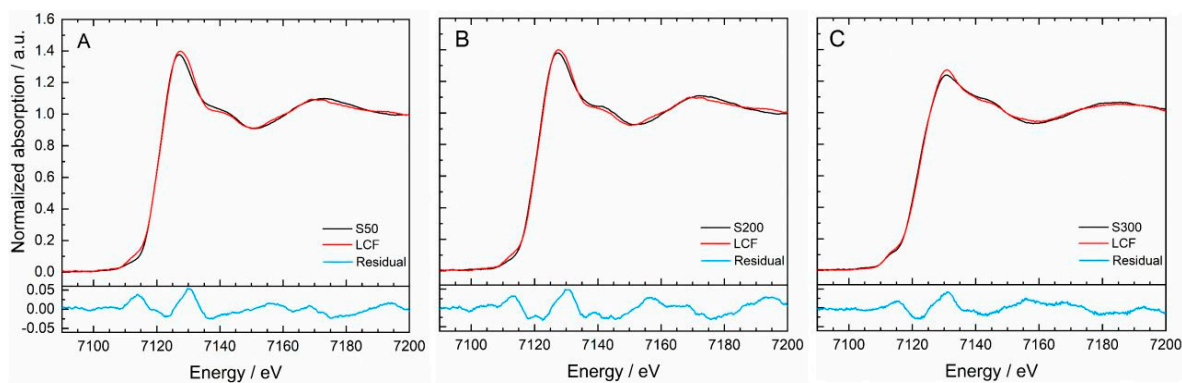


Figure A1. Best linear combination fits (LCF) (red), recorded Fe K-edge XANES spectra of the samples (black) and the respective residuals (blue). (A) LCF of sample S50 incorporates Fe foil (Fe⁰) and olivine (Fe^{II}). (B) LCF of sample S200 and (C) LCF of sample S300 based on Fe foil (Fe⁰), olivine (Fe^{II}) and magnetite (Fe^{II} & Fe^{III}).

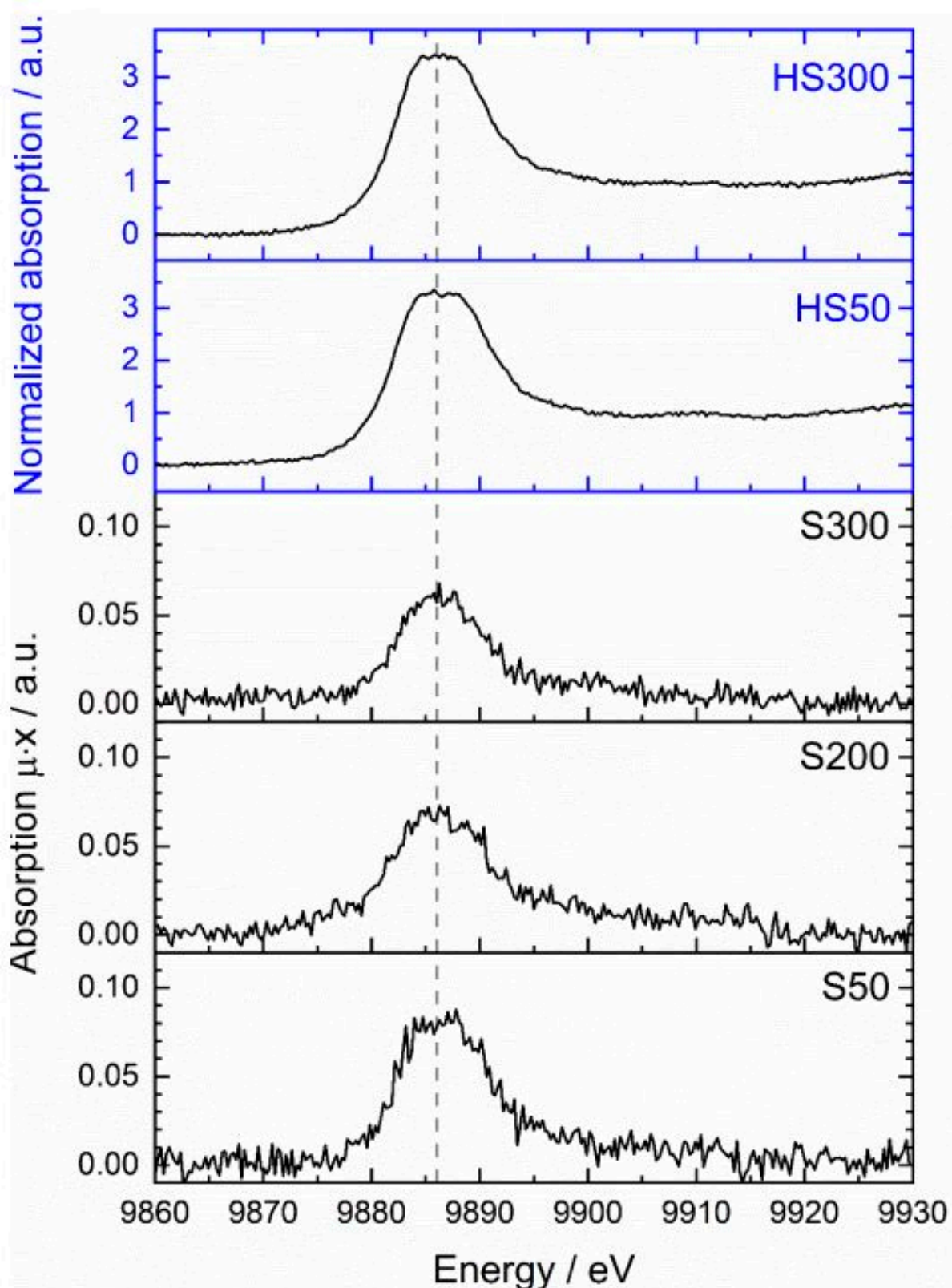


Figure A2. Ta L_{III}-edge XANES spectra of the high-Ta slag samples (HS50 and HS300) and the low-Ta slag samples (S50, S200, S300). The dashed vertical line indicates the common maximum at approx. 9886 eV.

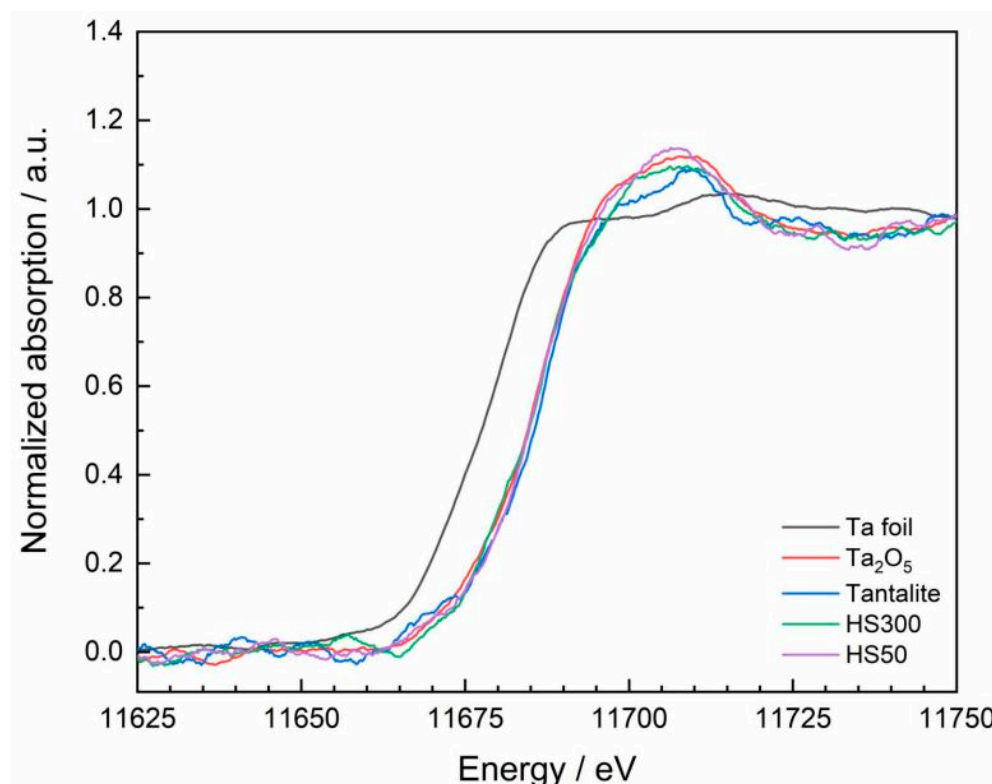


Figure A3. Ta LI-edge XANES spectra of the standard materials (Ta foil, Ta_2O_5 , tantalite) and the high-Ta slag samples (HS50 and HS300). The LI-edge of Ta0 is located at 11,681 eV. The measurements were performed as described in Section 3.3.1. Analogously, Si(110) was used as spherically bend crystal analyzer. The Ta LI-edge was probed in the energy range of 11,430–11,820 eV. In the post- and pre-edge region, the scanning parameters were set to energy steps of 2 eV and a measurement time of 2 s per step. The edge was scanned with energy steps of 0.25 eV and a measurement time of 4 s per step.

References

1. Directive 2012/19/EU of the European Parliament and of the Council of 4 July 2012 on Waste Electrical and Electronic Equipment (WEEE) (Recast) Text with EEA Relevance. 2012, Volume 197. Document 32012L0019. Available online: <https://eur-lex.europa.eu/LexUriServ/LexUriServ.do?uri=OJ:L:2012:197:0038:0071:en:PDF> (accessed on 29 January 2024).
2. Ebin, B.; Isik, M.I. Chapter 5—Pyrometallurgical Processes for the Recovery of Metals from WEEE. In *WEEE Recycling*; Chagnes, A., Cote, G., Ekberg, C., Nilsson, M., Retegan, T., Eds.; Elsevier: Amsterdam, The Netherlands, 2016; pp. 107–137. ISBN 978-0-12-803363-0.
3. Large-Scale WEEE Recycling Integrated in an Ore-Based Cu-Extraction System. *Journal of Sustainable Metallurgy*. Available online: <https://link.springer.com/article/10.1007/s40831-018-0157-5> (accessed on 26 September 2023).
4. Zhang, L.; Xu, Z. A Review of Current Progress of Recycling Technologies for Metals from Waste Electrical and Electronic Equipment. *J. Clean. Prod.* **2016**, *127*, 19–36. [[CrossRef](#)]
5. Alvear Flores, G.R.F.; Nikolic, S.; Mackey, P.J. ISASMELT™ for the Recycling of E-Scrap and Copper in the U.S. Case Study Example of a New Compact Recycling Plant. *J. Oper. Manag. (JOM)* **2014**, *66*, 823–832. [[CrossRef](#)]
6. Cardona, N.; Coursol, P.; Vargas, J.; Parra, R. The Physical Chemistry of Copper Smelting Slags and Copper Losses at the Paipote Smelter Part 2—Characterisation of Industrial Slags. *Can. Metall. Q.* **2011**, *50*, 330–340. [[CrossRef](#)]
7. Davenport, W.G.; King, M.; Schlesinger, M.; Biswas, A.K. Chemical Metallurgy of Copper Recycling. In *Extractive Metallurgy of Copper*; Elsevier: Amsterdam, The Netherlands, 2002; pp. 355–365. ISBN 978-0-08-044029-3.
8. Habashi, F. (Ed.) *Handbook of Extractive Metallurgy*; Wiley-VCH: Weinheim, NY, USA, 1998; Volume II, ISBN 978-3-527-28792-5.
9. Hagelüken, C. Recycling of Electronic Scrap at Umicore’s Integrated Metals Smelter and Refinery. *World Metall.—Erzmetall* **2006**, *59*, 152–161.
10. Isri Scrap Specifications Circular. 2017, pp. 1–67. Available online: <https://www.isrispecs.org/wp-content/uploads/2023/05/ISRI-Scrap-Specifications-Circular-updated-1.pdf> (accessed on 29 January 2024).

11. Latacz, D.; Diaz, F.; Birich, A.; Flerus, B.; Friedrich, B. WEEE Recycling at IME—RWTH Aachen: From Basic Metal Recovery to Resource Efficiency. Available online: <https://www.semanticscholar.org/paper/WEEE-Recycling-at-IME-%E2%80%93-RWTH-Aachen:-From-Basic-to-Latacz-Diaz/47c02905d5e9a9071e4bdac0ae7365f1b93ab5b1> (accessed on 7 July 2022).
12. Chen, M.; Avarmaa, K.; Taskinen, P.; Klemettinen, L.; Michallik, R.; O'Brien, H.; Jokilaakso, A. Handling Trace Elements in WEEE Recycling through Copper Smelting—an Experimental and Thermodynamic Study. *Miner. Eng.* **2021**, *173*, 107189. [[CrossRef](#)]
13. Yamane, L.H.; de Moraes, V.T.; Espinosa, D.C.R.; Tenório, J.A.S. Recycling of WEEE: Characterization of Spent Printed Circuit Boards from Mobile Phones and Computers. *Waste Manag.* **2011**, *31*, 2553–2558. [[CrossRef](#)]
14. Buchmann, M.; Borowski, N.; Leißner, T.; Heinig, T.; Reuter, M.A.; Friedrich, B.; Peuker, U.A. Evaluation of Recyclability of a WEEE Slag by Means of Integrative X-Ray Computer Tomography and SEM-Based Image Analysis. *Minerals* **2020**, *10*, 309. [[CrossRef](#)]
15. Nicol, S.; Hogg, B.; Mendoza, O.; Nikolic, S. Extraction and Recovery of Critical Metals from Electronic Waste Using ISASMELT™ Technology. *Processes* **2023**, *11*, 1012. [[CrossRef](#)]
16. Alvear, F.G.R.F.; Nikolic, S. ISASMELT™ for Recycling of Valuable Elements Contributing to a More Sustainable Society. In *REWAS 2013: Enabling Materials Resource Sustainability*; Kvithyld, A., Meskers, C., Kirchain, R., Krumdick, G., Mishra, B., Reuter, M., Wang, C., Schlesinger, M., Gaustad, G., Lados, D., et al., Eds.; Springer International Publishing: Cham, Switzerland, 2016; pp. 100–109. ISBN 978-3-319-48763-2.
17. Niu, X.; Li, Y. Treatment of Waste Printed Wire Boards in Electronic Waste for Safe Disposal. *J. Hazard. Mater.* **2007**, *145*, 410–416. [[CrossRef](#)]
18. Cui, J.; Zhang, L. Metallurgical Recovery of Metals from Electronic Waste: A Review. *J. Hazard. Mater.* **2008**, *158*, 228–256. [[CrossRef](#)] [[PubMed](#)]
19. Du, X.; Ma, Y. Phase Transformations during the Oxidation of Fayalite in Iron-Rich Nickel Slag. *Int. J. Mater. Res.* **2020**, *111*, 290–296. [[CrossRef](#)]
20. Mackwell, S.J. Oxidation Kinetics of Fayalite (Fe₂SiO₄). *Phys. Chem. Miner.* **1992**, *19*, 220–228. [[CrossRef](#)]
21. Calderón-Vásquez, I.; Segovia, V.; Cardemil, J.M.; Barraza, R. Assessing the Use of Copper Slags as Thermal Energy Storage Material for Packed-Bed Systems. *Energy* **2021**, *227*, 120370. [[CrossRef](#)]
22. Alkan, G.; Mechnich, P.; Lucas, H.; Knoblauch, N.; Sommerfeld, M.; Flucht, F.; Pernpeintner, J.; Sergeev, D.; Müller, M.; Friedrich, B. Assessment of Metallurgical Slags as Solar Heat Absorber Particles. *Minerals* **2022**, *12*, 121. [[CrossRef](#)]
23. Albrecht, S.; Cymorek, C.; Andersson, K.; Reichert, K.; Wolf, R. Tantalum and Tantalum Compounds. In *Ullmann's Encyclopedia of Industrial Chemistry*; John Wiley & Sons, Ltd.: Hoboken, NJ, USA, 2011; ISBN 978-3-527-30673-2.
24. Bakhsheshi-Rad, H.R.; Najafinezhad, A.; Hamzah, E.; Ismail, A.F.; Berto, F.; Chen, X. Clinoenstatite/Tantalum Coating for Enhancement of Biocompatibility and Corrosion Protection of Mg Alloy. *J. Funct. Biomater.* **2020**, *11*, 26. [[CrossRef](#)]
25. Barume, B.; Naeher, U.; Ruppen, D.; Schütte, P. Conflict Minerals (3TG): Mining Production, Applications and Recycling. *Curr. Opin. Green Sustain. Chem.* **2016**, *1*, 8–12. [[CrossRef](#)]
26. Cardarelli, F.; Taxil, P.; Savall, A. Tantalum Protective Thin Coating Techniques for the Chemical Process Industry: Molten Salts Electrocoating as a New Alternative. *Int. J. Refract. Met. Hard Mater.* **1996**, *14*, 365–381. [[CrossRef](#)]
27. Cardonne, S.M.; Kumar, P.; Michaluk, C.A.; Schwartz, H.D. Tantalum and Its Alloys. *Int. J. Refract. Met. Hard Mater.* **1995**, *13*, 187–194. [[CrossRef](#)]
28. Lindagato, P.; Li, Y.; Yang, G. Save the Giants: Demand beyond Production Capacity of Tantalum Raw Materials. *Min. Econ.* **2023**, *36*, 535–541. [[CrossRef](#)]
29. Zednicek, T. Tantalum Capacitors in 5G Infrastructure. What are critical metals? *Tantalum-Niobium Int. Study Cent.* **2023**, *184*, 35.
30. Schwich, L.; Küpers, M.; Finsterbusch, M.; Schreiber, A.; Fattakhova-Rohlfing, D.; Guillon, O.; Friedrich, B. Recycling Strategies for Ceramic All-Solid-State Batteries—Part I: Study on Possible Treatments in Contrast to Li-Ion Battery Recycling. *Metals* **2020**, *10*, 1523. [[CrossRef](#)]
31. Chen, L.; Lin, X.; Dang, W.; Huang, H.; Liu, G.; Yang, Z. Tantalum Oxide Nanosheets/Polypropylene Composite Separator Constructing Lithium-Ion Channels for Stable Lithium Metal Batteries. *Adv. Compos. Hybrid Mater.* **2022**, *6*, 12. [[CrossRef](#)]
32. Fujita, T.; Ono, H.; Dodbiba, G.; Yamaguchi, K. Evaluation of a Recycling Process for Printed Circuit Board by Physical Separation and Heat Treatment. *Waste Manag.* **2014**, *34*, 1264–1273. [[CrossRef](#)]
33. Riedewald, F.; Povey, I.; Barton, K.; Lewis, L.; Santos, S.; O'Mahoney, M.; Sousa-Gallagher, M. Tantalum Capacitor Separation from Waste Printed Circuit Boards with Molten Salt or Metal. *Chem. Ing. Tech.* **2022**, *95*, 944–949. [[CrossRef](#)]
34. Niu, B.; Chen, Z.; Xu, Z. Method for Recycling Tantalum from Waste Tantalum Capacitors by Chloride Metallurgy. *ACS Sustain. Chem. Eng.* **2017**, *5*, 1376–1381. [[CrossRef](#)]
35. Niu, B.; Chen, Z.; Xu, Z. Recovery of Tantalum from Waste Tantalum Capacitors by Supercritical Water Treatment. *ACS Sustain. Chem. Eng.* **2017**, *5*, 4421–4428. [[CrossRef](#)]
36. Wajima, T. Decomposition of Mould Resin in Spent Capacitors by NaOH for the Recovery of Tantalum. *Int. J. Environ. Sustain. Dev.* **2017**, *8*, 285–289. [[CrossRef](#)]
37. Agrawal, M.; Singh, K.K.; Singh, R. Hydrometallurgical Recovery of Manganese and Nickel and Isolation of Tantalum from Obsolete Tantalum Capacitor. *J. Environ. Chem. Eng.* **2022**, *10*, 108887. [[CrossRef](#)]

38. Matsuoka, R.; Mineta, K.; Okabe, T.H. Recycling Process for Tantalum and Some Other Metal Scraps. 2004. Available online: <https://citeseerx.ist.psu.edu/document?repid=rep1&type=pdf&doi=25220b5dcc7f278125d6c5fb9e13bbdb5331609f> (accessed on 29 January 2024).
39. Spitzczok von Brisinski, L.; Goldmann, D.; Endres, F. Recovery of Metals from Tantalum Capacitors with Ionic Liquids. *Chem. Ing. Tech.* **2014**, *86*, 196–199. [[CrossRef](#)]
40. Micheau, C.; Arrachart, G.; Turgis, R.; Lejeune, M.; Draye, M.; Michel, S.; Legeai, S.; Pellet-Rostaing, S. Ionic Liquids as Extraction Media in a Two-Step Eco-Friendly Process for Selective Tantalum Recovery. *ACS Sustain. Chem. Eng.* **2020**, *8*, 1954–1963. [[CrossRef](#)]
41. Chen, W.-S.; Ho, H.-J.; Lin, K.-Y. Hydrometallurgical Process for Tantalum Recovery from Epoxy-Coated Solid Electrolyte Tantalum Capacitors. *Materials* **2019**, *12*, 1220. [[CrossRef](#)]
42. Swain, B.; Lee, J.; Woo Gu, B.; Lee, C.-G.; Yoon, J.-H. Sustainable Valorization of Semiconductor Industry Tantalum Scrap Using Non-Hazardous HF Substitute Lixiviant. *Waste Manag.* **2022**, *144*, 294–302. [[CrossRef](#)] [[PubMed](#)]
43. de Oliveira, J.M.; Anes, I.A.; Coleti, J.L.; Espinosa, D.C.R.; de Carvalho, M.S.; Tenório, J.A.S. Niobium and Tantalum Recovery from the Primary Source and from Tin Slag, an Industrial Challenge: A Review. *Can. J. Chem. Eng.* **2023**, *101*, 1743–1761. [[CrossRef](#)]
44. Allain, E.; Kanari, N.; Diot, F.; Yvon, J. Development of a Process for the Concentration of the Strategic Tantalum and Niobium Oxides from Tin Slags. *Miner. Eng.* **2019**, *134*, 97–103. [[CrossRef](#)]
45. Xie, K.; Wei, X.; Ye, L.; Wan, M.; Li, S.; Wu, J. Recovery and Preparation of Potassium Fluorotantalate from High-Tantalum-Bearing Waste Slag by Pressure Alkaline Decomposition. *Metals* **2022**, *12*, 648. [[CrossRef](#)]
46. Lee, Y.; Yoo, B.; Nersisyan, H.H.; Lee, J.-H. Temperature and Concentration Dependencies of LiF-NaF-K₂TaF₇ Phase Equilibria and Effects on Ta Electrodeposition Layer. *J. Electrochem. Soc.* **2018**, *165*, D432–D438. [[CrossRef](#)]
47. Gaballah, I.; Allain, E. Recycling of Strategic Metals from Industrial Slag by a Hydro-and Pyrometallurgical Process. *Resour. Conserv. Recycl.* **1994**, *10*, 75–85. [[CrossRef](#)]
48. Brocchi, E.A.; Moura, F.J. Chlorination Methods Applied to Recover Refractory Metals from Tin Slags. *Miner. Eng.* **2008**, *21*, 150–156. [[CrossRef](#)]
49. Generowicz, N.; Kulczycka, J. Recovery of Tantalum from Different Resources. *Archit. Civ. Eng. Environ.* **2020**, *13*, 79–84. [[CrossRef](#)]
50. Magdalena, R.; Valero, A.; Calvo, G.; Alguacil, F.J.; López, F.A. Simulation to Recover Niobium and Tantalum from the Tin Slags of the Old Penouta Mine: A Case Study. *Minerals* **2021**, *11*, 1123. [[CrossRef](#)]
51. Nieberl, M.; Hornung, A.; Sajdak, M.; Majewski, A.J.; Ouadi, M. Application and Recycling of Tantalum from Waste Electric and Electronic Equipment—A Review. *Resour. Conserv. Recycl.* **2023**, *190*, 106866. [[CrossRef](#)]
52. Mackay, D.A.R.; Simandl, G.J. Geology, Market and Supply Chain of Niobium and Tantalum—A Review. *Min. Depos.* **2014**, *49*, 1025–1047. [[CrossRef](#)]
53. Gaballah, I.; Allain, E.; Djona, M. Extraction of Tantalum and Niobium from Tin Slags by Chlorination and Carbochlorination. *Met. Mater. Trans. B* **1997**, *28*, 359–369. [[CrossRef](#)]
54. Tian, E.; Xie, L.; Wang, R.; Duan, X.; Huang, F.; Che, X.; Chen, X.; Wang, L. Mineralogical Constraints on Nb-Ta Fractionation in Early Cretaceous A-Type Granites from the Suzhou Pluton, SE China. *Lithos* **2021**, *402–403*, 106286. [[CrossRef](#)]
55. Stepanov, A.; Mavrogenes, J.A.; Meffre, S.; Davidson, P. The Key Role of Mica during Igneous Concentration of Tantalum. *Contrib. Miner. Pet.* **2014**, *167*, 1009. [[CrossRef](#)]
56. Moore, R.O.; Griffin, W.L.; Gurney, J.J.; Ryan, C.G.; Cousens, D.R.; Sie, S.H.; Suter, G.F. Trace Element Geochemistry of Ilmenite Megacrysts from the Monastery Kimberlite, South Africa. *Lithos* **1992**, *29*, 1–18. [[CrossRef](#)]
57. Adelman, C.; Delabie, A.; Schepers, B.; Rodriguez, L.N.J.; Franquet, A.; Conard, T.; Opsomer, K.; Vaesen, I.; Moussa, A.; Pourtois, G.; et al. Atomic Layer Deposition of Tantalum Oxide and Tantalum Silicate from Chloride Precursors. *Chem. Vap. Depos.* **2012**, *18*, 225–238. [[CrossRef](#)]
58. Reeve, D.A.; Bright, N.F.H. Phase Relations in the System CaO-Ta₂O₅-SiO₂. *J. Am. Ceram. Soc.* **1969**, *52*, 405–409. [[CrossRef](#)]
59. Shannon, R.D. Revised Effective Ionic Radii and Systematic Studies of Interatomic Distances in Halides and Chalcogenides. *Acta Crystallogr. Sect. A* **1976**, *32*, 751–767. [[CrossRef](#)]
60. Okrusch, M.; Matthes, S. Eine Einführung in die spezielle Mineralogie, Petrologie und Lagerstättenkunde. In *Mineralogie*; Springer Spektrum: Berlin, Germany, 2014; ISBN 978-3-642-34660-6.
61. Guevarra, J.; van Smaalen, S.; Daniels, P.; Rotiroti, N.; Lichtenberg, F. Perovskite-Related Ca(Nb,Ti)O_{3,33}. *Z. Für Krist.—Cryst. Mater.* **2005**, *220*, 19–24. [[CrossRef](#)]
62. Kamba, S.; Petzelt, J.; Buixaderas, E.; Haubrich, D.; Vaněk, P.; Kužel, P.; Jawahar, I.N.; Sebastian, M.T.; Mohanan, P. High Frequency Dielectric Properties of A₅B₄O₁₅ Microwave Ceramics. *J. Appl. Phys.* **2001**, *89*, 3900–3906. [[CrossRef](#)]
63. Ubic, R.; Merry, J.C.; Leach, A.C. Electron Microscopy of Lead and Calcium Pyrochlores. *J. Eur. Ceram. Soc.* **2004**, *24*, 1725–1728. [[CrossRef](#)]
64. Feng, D.; Navrotsky, A. Thermochemistry of Rare Earth Perovskites. *MRS Adv.* **2016**, *1*, 2695–2700. [[CrossRef](#)]
65. Bartelmy, D. Webmineral Mineralogy Database. Available online: <https://www.webmineral.com/> (accessed on 29 January 2024).
66. Gupta, S. Introduction to Ferroelectrics and Related Materials. In *Ferroelectric Materials for Energy Harvesting and Storage*; Elsevier: Amsterdam, The Netherlands, 2021; pp. 1–41. ISBN 978-0-08-102802-5.

67. Schirmer, T.; Qiu, H.; Goldmann, D.; Stallmeister, C.; Friedrich, B. Influence of P and Ti on Phase Formation at Solidification of Synthetic Slag Containing Li, Zr, La, and Ta. *Minerals* **2022**, *12*, 310. [[CrossRef](#)]
68. Peters, E.; Müller-Buschbaum, H. Ein Titan-Tantaloxid Mit Ti^{II} : $Ti_{0,33} Ta_{0,67} O_2$ ($TiTa_2O_6$)/A Titanium Tantalum Oxide of Ti^{II} : $Ti_{0,33} Ta_{0,67} O_2$ ($TiTa_2O_6$). *Z. Für Naturforschung B* **1995**, *50*, 1167–1170. [[CrossRef](#)]
69. Okrusch, M.; Matthes, S. *Mineralogie Eine Einführung in Die Spezielle Mineralogie, Petrologie und Lagerstättenkunde*; Springer: Berlin/Heidelberg, Germany, 2009; ISBN 978-3-540-78200-1.
70. Bodinier, J.-I.; Merlet, C.; Bedini, R.M.; Simien, F.; Remaidi, M.; Garrido, C.J. Distribution of Niobium, Tantalum, and Other Highly Incompatible Trace Elements in the Lithospheric Mantle: The Spinel Paradox. *Geochim. Cosmochim. Acta* **1996**, *60*, 545–550. [[CrossRef](#)]
71. Chen, J. *Advances in High-Pressure Technology for Geophysical Applications*, 1st ed.; Elsevier: Amsterdam, The Netherlands; Boston, MA, USA, 2005; ISBN 978-0-444-51979-5.
72. O'Neill, H. Quartz-Fayalite-Iron and Quartz-Fayalite-Magnetite Equilibria and the Free Energy of Formation of Fayalite (Fe_2SiO_4) and Magnetite (Fe_3O_4). *Am. Mineral.* **1987**, *72*, 67–75.
73. Chen, S.Y.; Chu, M.S. A New Process for the Recovery of Iron, Vanadium, and Titanium from Vanadium Titanomagnetite. *J. South. Afr. Inst. Min. Metall.* **2014**, *114*, 481–488.
74. Schoenthal, W.; Liu, X.; Cox, T.; Mesa, J.L.; Maicas, M.; Diaz-Michelena, M.; Laughlin, D.E.; McHenry, M.E. Synthesis and Magnetic Properties of Single Phase Titanomagnetites. *J. Appl. Phys.* **2014**, *115*, 17A934. [[CrossRef](#)]
75. Bale, C.W.; Bélisle, E.; Chartrand, P.; Decterov, S.A.; Eriksson, G.; Gheribi, A.E.; Hack, K.; Jung, I.-H.; Kang, Y.-B.; Melançon, J.; et al. FactSage Thermochemical Software and Databases, 2010–2016. *Calphad* **2016**, *54*, 35–53. [[CrossRef](#)]
76. Seidler, G.T.; Mortensen, D.R.; Remesnik, A.J.; Pacold, J.I.; Ball, N.A.; Barry, N.; Styczinski, M.; Hoidn, O.R. A Laboratory-Based Hard X-ray Monochromator for High-Resolution X-ray Emission Spectroscopy and x-Ray Absorption near Edge Structure Measurements. *Rev. Sci. Instrum.* **2014**, *85*, 113906. [[CrossRef](#)]
77. Seddon-Ferretti, M.E.; Mottram, L.M.; Stennett, M.C.; Corkhill, C.L.; Hyatt, N.C. HERMES—A GUI-Based Software Tool for Pre-Processing of X-Ray Absorption Spectroscopy Data from Laboratory Rowland Circle Spectrometers. *J. Synchrotron Rad.* **2022**, *29*, 276–279. [[CrossRef](#)] [[PubMed](#)]
78. Bearden, J.A.; Burr, A.F. Reevaluation of X-Ray Atomic Energy Levels. *Rev. Mod. Phys.* **1967**, *39*, 125–142. [[CrossRef](#)]
79. Ravel, B.; Newville, M. ATHENA, ARTEMIS, HEPHAESTUS: Data Analysis for X-Ray Absorption Spectroscopy Using IFEFFIT. *J. Synchrotron Rad.* **2005**, *12*, 537–541. [[CrossRef](#)]
80. Smith, D.K.; Jenkins, R. The Powder Diffraction File: Past, Present, and Future. *J. Res. Natl. Inst. Stand. Technol.* **1996**, *101*, 259. [[CrossRef](#)]
81. Vaitkus, A.; Merkys, A.; Gražulis, S. Validation of the Crystallography Open Database Using the Crystallographic Information Framework. *J. Appl. Crystallogr.* **2021**, *54*, 661–672. [[CrossRef](#)]
82. Jain, A.; Ong, S.P.; Hautier, G.; Chen, W.; Richards, W.D.; Dacek, S.; Cholia, S.; Gunter, D.; Skinner, D.; Ceder, G.; et al. Commentary: The Materials Project: A Materials Genome Approach to Accelerating Materials Innovation. *APL Mater.* **2013**, *1*, 011002. [[CrossRef](#)]
83. Jercinovic, M.J.; Williams, M.L.; Allaz, J.; Donovan, J.J. Trace Analysis in EPMA. *IOP Conf. Ser. Mater. Sci. Eng.* **2012**, *32*, 012012. [[CrossRef](#)]
84. Merlet, C. Quantitative Electron Probe Microanalysis: New Accurate Φ (Pz) Description. In *Electron Microbeam Analysis*; Boekestein, A., Pavićević, M.K., Eds.; Springer Vienna: Vienna, Austria, 1992; Volume 12, pp. 107–115. ISBN 978-3-211-82359-0.
85. Sasabe, M.; Jibiki, M. Permeability of Oxygen Through Molten Slag Containing Iron Oxide. *Can. Metall. Q.* **1983**, *22*, 29–36. [[CrossRef](#)]
86. Sasabe, M. Atsushi Asamura Transport Phenomenon of Oxygen through Molten Slags. In *Second International Symposium on Metallurgical Slags and Fluxes: Proceedings of the Second International Symposium on Metallurgical Slags and Fluxes*; Fine, H.A., Gaskell, D.R., Metallurgical Society of AIME, Eds.; The Society: Warrendale, PA, USA, 1984; pp. 651–668. ISBN 978-0-89520-483-7.
87. Sasabe, M.; Goto, K.S. Permeability, Diffusivity, and Solubility of Oxygen Gas in Liquid Slag. *Met. Trans. B* **1974**, *5*, 2225–2233. [[CrossRef](#)]
88. Jacob, K.T.; Kale, G.M.; Iyengar, G.N.K. Chemical Potentials of Oxygen for Fayalite-Quartz-Iron and Fayalite-Quartz-Magnetite Equilibria. *Metall. Trans. B* **1989**, *20*, 679–685. [[CrossRef](#)]
89. Alhajri, N.S.; Yoshida, H.; Anjum, D.H.; Garcia-Esparza, A.T.; Kubota, J.; Domen, K.; Takanahe, K. Synthesis of Tantalum Carbide and Nitride Nanoparticles Using a Reactive Mesoporous Template for Electrochemical Hydrogen Evolution. *J. Mater. Chem. A* **2013**, *1*, 12606. [[CrossRef](#)]
90. Martin, R.F.; Wülser, P.-A. Niobium and Tantalum in Minerals: Siderophile, Chalcophile or Lithophile, and Polyvalent. *J. Geochem. Explor.* **2014**, *147*, 16–25. [[CrossRef](#)]
91. Evans, J. *X-ray Absorption Spectroscopy for the Chemical and Materials Sciences*, 1st ed.; Wiley: Hoboken, NJ, USA, 2018; ISBN 978-1-119-99091-8.
92. Tougerti, A.; Cristol, S.; Berrier, E.; Briois, V.; La Fontaine, C.; Villain, F.; Joly, Y. XANES Study of Rhenium Oxide Compounds at the L_1 and L_3 Absorption Edges. *Phys. Rev. B* **2012**, *85*, 125136. [[CrossRef](#)]
93. Fittschen, U.; Guilherme, A.; Böttger, S.; Rosenberg, D.; Menzel, M.; Jansen, W.; Busker, M.; Gotlib, Z.P.; Radtke, M.; Riesemeier, H.; et al. A Setup for Synchrotron-Radiation-Induced Total Reflection X-ray Fluorescence and X-ray Absorption near-Edge Structure Recently Commissioned at BESSY II BAMline. *J. Synchrotron Rad.* **2016**, *23*, 820–824. [[CrossRef](#)]

94. Cartier, C.; Hammouda, T.; Boyet, M.; Mathon, O.; Testemale, D.; Moine, B.N. Evidence for Nb²⁺ and Ta³⁺ in Silicate Melts under Highly Reducing Conditions: A XANES Study. *Am. Mineral.* **2015**, *100*, 2152–2158. [[CrossRef](#)]
95. Asakura, H.; Shishido, T.; Yamazoe, S.; Teramura, K.; Tanaka, T. Structural Analysis of Group V, VI, and VII Metal Compounds by XAFS. *J. Phys. Chem. C* **2011**, *115*, 23653–23663. [[CrossRef](#)]
96. Farges, F.; Linnen, R.L.; Brown, G.E. Redox and Speciation of Tin in Hydrous Silicate Glasses: A Comparison with Nb, Ta, Mo and W. *Can. Mineral.* **2006**, *44*, 795–810. [[CrossRef](#)]
97. Burnham, A.D.; Berry, A.J.; Wood, B.J.; Cibin, G. The Oxidation States of Niobium and Tantalum in Mantle Melts. *Chem. Geol.* **2012**, *330–331*, 228–232. [[CrossRef](#)]
98. Yamazoe, S.; Hitomi, Y.; Shishido, T.; Tanaka, T. XAFS Study of Tungsten L₁- and L₃-Edges: Structural Analysis of WO₃ Species Loaded on TiO₂ as a Catalyst for Photo-Oxidation of NH₃. *J. Phys. Chem. C* **2008**, *112*, 6869–6879. [[CrossRef](#)]
99. Marcus, M.A.; Westphal, A.J.; Fakra, S.C. Classification of Fe-Bearing Species from K -Edge XANES Data Using Two-Parameter Correlation Plots. Erratum. *J. Synchrotron Rad.* **2009**, *16*, 439. [[CrossRef](#)]
100. Prietzel, J.; Thieme, J.; Eusterhues, K.; Eichert, D. Iron Speciation in Soils and Soil Aggregates by Synchrotron-based X-ray Microspectroscopy (XANES, μ -XANES). *Eur. J Soil Sci.* **2007**, *58*, 1027–1041. [[CrossRef](#)]
101. Davis, B.L. Semiquantitative XRD Analysis with the Aid of Reference Intensity Ratio Estimates. *Powder Diffr.* **1998**, *13*, 185–187. [[CrossRef](#)]

Disclaimer/Publisher’s Note: The statements, opinions and data contained in all publications are solely those of the individual author(s) and contributor(s) and not of MDPI and/or the editor(s). MDPI and/or the editor(s) disclaim responsibility for any injury to people or property resulting from any ideas, methods, instructions or products referred to in the content.